Chem Soc Rev

REVIEW ARTICLE

View Article Online
View Journal | View Issue

Open Access Article. Published on 28 August 2015. Downloaded on 2/9/2026 4:13:16 PM.
This article is licensed under a Creative Commons Attribution 3.0 Unported Licence.

Cite this: *Chem. Soc. Rev.*, 2015, **44**, 8326

Received 28th April 2015

DOI: 10.1039/c5cs00352k

www.rsc.org/chemsocrev

# Doping of $TiO_2$ for sensitized solar cells

Bart Roose,[a] Sandeep Pathak*[b] and Ullrich Steiner*[a]

This review gives a detailed summary and evaluation of the use of $TiO_2$ doping to improve the performance of dye sensitized solar cells. Doping has a major effect on the band structure and trap states of $TiO_2$, which in turn affect important properties such as the conduction band energy, charge transport, recombination and collection. The defect states of $TiO_2$ are highly dependent on the synthesis method and thus the effect of doping may vary for different synthesis techniques, making it difficult to compare the suitability of different dopants. High-throughput methods may be employed to achieve a rough prediction on the suitability of dopants for a specific synthesis method. It was however found that nearly every employed dopant can be used to increase device performance, indicating that the improvement is not so much caused by the dopant itself, as by the defects it eliminates from $TiO_2$. Furthermore, with the field shifting from dye sensitized solar cells to perovskite solar cells, the role doping can play to further advance this emerging field is also discussed.

## 1 Introduction

To keep up with the future demand for energy it will be necessary to deploy clean, renewable sources on a massive scale.[1,2] One promising option is the large scale application of photovoltaic devices, which generate electricity directly from sun light.[3] This has so far been limited because of the high cost associated with the production of these devices.[2,4,5] In the last decades many new photovoltaic technologies have been developed, promising low cost, high-throughput processing which will pave the way to affordable renewable energy.[1,2,5,6] One of the leading candidates is the dye sensitized solar cell (DSSC),[7–9] in particular the perovskite-based solar cell, which is closely related to devices employing

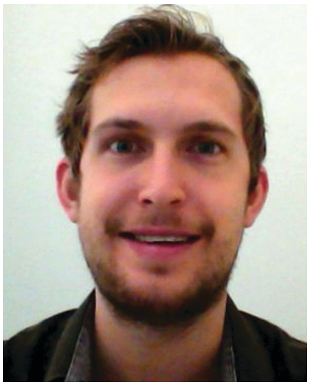

**Bart Roose**

*Bart Roose graduated in chemistry from the Radboud University Nijmegen in 2013. He then went on with his doctoral research in the group of Prof. Ullrich Steiner at the University of Cambridge and the Adolphe Merkle Institute in Fribourg, Switzerland. His research interests include nano-structured metal oxides, doping of metal oxides and sensitized solar cells.*

**Sandeep Pathak**

*Sandeep Pathak gained his PhD at the University of Cambridge, UK in 2011, working on High Temperature Superconductors with Prof. David Cardwell. He spent two years at the Clarendon Laboratory (University of Oxford, UK) with Prof. Henry Snaith as a post doc working on Dye-Sensitized Solar Cells. He then joined Prof. Ullrich Steiner at Cavendish Laboratory (University of Cambridge, UK) and continued to work on photovoltaic devices as research associate. He moved back to Clarendon Laboratory (Oxford University, UK) to work with Prof. Henry Snaith, as a senior research associate in October 2013 and since then his research activities remained focussed on the perovskite solar cells. His current research work predominantly involves development of new material structures for perovskite solar cells. Subsequently, understanding their photo-physical properties and controlling the physical processes occurring at the electronic interfaces.*

---

[a] *Adolphe Merkle Institute, Rue des Verdiers, CH-1700 Fribourg, Switzerland. E-mail: ullrich.steiner@unifr.ch*

[b] *Clarendon Laboratory, Department of Physics, University of Oxford, Parks Road, Oxford, OX1 3PU, UK*

This journal is © The Royal Society of Chemistry 2015

Open Access Article. Published on 28 August 2015. Downloaded on 2/9/2026 4:13:16 PM.
This article is licensed under a Creative Commons Attribution 3.0 Unported Licence.

organic dyes.[10–13] Perovskite solar cells currently have a NREL certified record efficiency of more than 20%,[6] with a marked upward trend. This is in the efficiency range needed for commercially viable applications.[14]

Major challenges remain however in scaling up the fabrication from the laboratory to industrial production,[15,16] addressing toxicity issues,[17–19] reducing hysteresis[17,20,21] and in particular regarding the achievement of sufficiently high device lifetimes.[13,20] The control over the device properties and how they can be reliably achieved requires a better understanding of the underlying chemistry and physics. Ever since the first report of DSSCs, best performing devices have relied on titanium dioxide ($TiO_2$) as nanostructured electron transporting layer and/or hole blocking layer.[22,23] Extensive research has been done to control the morphology of the $TiO_2$ with the aim of maximizing the dye–$TiO_2$ interface area and light absorption.[24–26] With the recent optimization of dyes, hole-conductors and device architectures the focus has shifted to controlling the electronic properties of $TiO_2$. Mesoporous $TiO_2$ is full of lattice defects that arise during synthesis, resulting in a multitude of electronic sub-band gap states that are able to trap charges.[8,9]

Here we discuss how these defects affect the electronic properties of $TiO_2$ and how they can be influenced by doping, that is by deliberately introducing impurities into $TiO_2$. In photocatalytic materials this is a well known method to increase the spectral response and promote the separation of charges.[27–29] From these studies it is evident that not only the type of dopant is important but also where the dopant is situated in the $TiO_2$-lattice. Another way to control recombination processes is to cover $TiO_2$ with a thin layer of insulating oxide,[30] this is however outside the scope of this review.

First the general working principle of DSSCs and the properties of $TiO_2$ are elucidated. This is followed by a detailed overview of results that have been achieved so far using different dopants and doping techniques. Then, we assess what can be learned from these doping studies and how doping can be implemented to achieve better performance in perovskite solar cells. Finally, the tools that can be used to investigate the (electronic) properties of $TiO_2$ and the effects of doping are summarized.

**Ullrich Steiner**

*Ullrich (Ulli) Steiner studied physics at the University of Konstanz, Germany. He gained his PhD in 1993, working with Prof. J Klein and Prof. G. Schatz at the Weizmann Institute, Israel. After post-doc positions at the Weizmann Institute and the Institute Charles Sadron, France, he returned to Konstanz where he finished his Habilitation in 1998. He joined the faculty of the University of Groningen as full professor in 1999 and became the John Humphrey Plummer Professor of Physics of Materials at the University of Cambridge in 2004. Since 2014, he holds the chair of Soft Matter Physics at the Adolphe Merkle Institute in Switzerland.*

## 2 Working principle of DSSCs

The first working example of a DSSC was reported by O'Regan and Grätzel in 1991.[7] The same device architecture is still employed today and consists of the following components (top to bottom of Fig. 1a):

- Transparent conducting oxide (TCO) coated glass. Typical TCOs are tin-doped indium oxide (ITO) and fluorine-doped tin oxide (FTO).
- Hole blocking layer (HBL), a continuous layer of a metal oxide that prevents holes from reaching the TCO, shorting the device.
- Electron transporting material consisting of a mesoporous metal oxide, which is usually $TiO_2$. Several other metal oxides such as $SnO_2$,[31] ZnO[32,33] and $SrTiO_3$[34] have also been explored, but none of them perform as well as $TiO_2$.
- Dye adsorbed to the mesoporous metal oxide, which is responsible for absorbing light. Because the adsorbed dye usually consists of only a monolayer, a several micrometer thick mesoporous layer is needed to provide sufficient surface area to absorb most of the light.
- Liquid electrolyte or solid-state hole transporting material (HTM), which is infiltrated into the mesoporous layer. Liquid electrolytes often contain the iodide/triiodide redox couple. A problem using liquid electrolytes is the possible leakage of the corrosive fluid. Solid-state HTMs do not suffer from this problem but feature lower device efficiencies. A typical HTM is 2,2′,7,7′-tetrakis(*N*,*N*′-di-*p*-methoxyphenylamine)-9,9′-spirobifluorene (spiro-OMeTAD).
- Back contact consisting of a metal electrode.

When the device is illuminated the dye is excited, promoting electrons from the highest occupied molecular orbital (HOMO) to the lowest unoccupied molecular orbital (LUMO). This excited state injects electrons into the conduction band (CB) of $TiO_2$, which diffuse through the mesoporous scaffold to the TCO. The holes are transferred from the HOMO of the dye to the HTM and from there to the back electrode (Fig. 1b).

The three important quantities governing the efficiency of a solar cell are the short circuit current $J_{SC}$, the open circuit voltage $V_{OC}$ and the fill factor FF. $J_{SC}$ is the current through the device in the absence of a net voltage, that is for a short-circuited device. It is highly dependent on light absorption and charge collection efficiency. $V_{OC}$ is the voltage across the device in the absence of a net current. It depends on the energy difference between the Fermi levels ($E_F$) of the $TiO_2$ CB and HTM valence band (VB) or HOMO, and on recombination processes. The fill factor quantifies the power that can be delivered by the device. It is defined by dividing the maximum power output by $J_{SC} \times V_{OC}$. Its magnitude depends on series and shunt resistances in the device. A low series resistance and high shunt resistance minimize internal losses, thereby maximizing the power output of the device.

Open Access Article. Published on 28 August 2015. Downloaded on 2/9/2026 4:13:16 PM.
This article is licensed under a Creative Commons Attribution 3.0 Unported Licence.

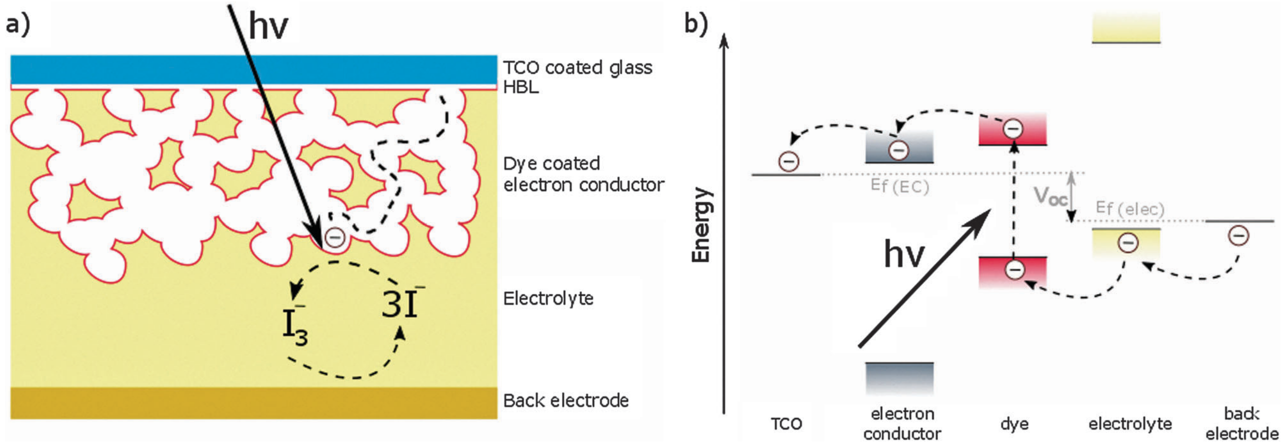

Fig. 1 (a) Schematic of DSSC device architecture, consisting of (top to bottom): transparent conducting oxide (TCO) coated glass; continuous metal oxide hole blocking layer (HBL); electron conductor coated with dye; liquid electrolyte or solid-state hole transporting material (HTM); metal back electrode. Upon the absorption of light, electrons and holes are created, which are transported through the respective transporting materials to the electrodes. (b) Charge transport in a DSSC: upon absorption of light by the dye, an electron is excited from the HOMO to the LUMO, injected into the CB of the electron conductor ($TiO_2$) and transported to the TCO electrode. The dye is regenerated by oxidation of iodide to tri-iodide. In the case of a sold-state HTM, the hole is transported through the HTM to the electrode.

To obtain maximum efficiencies, it is important to match the CB of $TiO_2$ to the LUMO of the dye so that the potential difference is sufficiently large for electron injection, while keeping the difference between the CB of $TiO_2$ and the VB of the HTM as large as possible to maximize $V_{OC}$.

## 3 $TiO_2$

The large band gap, suitable band edge levels for charge injection and extraction, the long lifetime of excited electrons, exceptional resistance to photo corrosion, non-toxicity and low cost have made $TiO_2$ a popular material for solar energy applications.[27–29]

$TiO_2$ occurs naturally in three crystalline forms; anatase (tetragonal), rutile (tetragonal) and brookite (orthorhombic). For DSSCs, anatase is the most commonly used phase due to its superior charge transport. The tetragonal anatase crystal structure is made up of a chain of distorted $TiO_6$ octahedrons, which results in a unit cell containing four Ti atoms (at positions $[0,0,0]$, $[\frac{1}{2},\frac{1}{2},\frac{1}{2}]$, $[0,\frac{1}{2},\frac{1}{4}]$ and $[\frac{1}{2},0,\frac{3}{4}]$) and eight O atoms[26,35,36] (Fig. 2).

$TiO_2$ prepared by sol–gel processes is amorphous and annealing at elevated temperatures is required to achieve the desired crystal structure. The crystallization temperature is limited by the anatase–rutile transition. Since rutile is the thermodynamically most stable polymorph of $TiO_2$ at all temperatures, the anatase to rutile transition temperature depends sensitively on preparation conditions. Because of their different band structures, mixed phases of anatase and rutile generally cause the trapping of charge carriers and promote recombination processes. They are mostly undesirable in DSSC electrodes, although there are some studies suggesting a small amount of rutile nanoparticles can enhance device performance.[37–39] DSSCs employing rutile $TiO_2$ generally suffer from a lower CB compared to anatase, leading to a lower $V_{OC}$. In addition, reduced dye adsorption and charge transport lower the obtainable $J_{SC}$.[40–42]

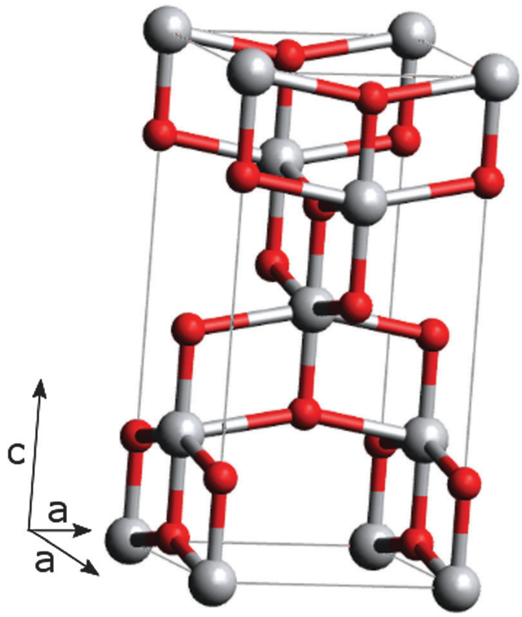

Fig. 2 The anatase unit cell; titanium atoms are grey, oxygen atoms are red. Oxygen atoms form a distorted octahedron with a titanium atom at the center, which is clearly illustrated for the central titanium atom.

Because of these complications, rutile is not frequently used in DSSCs, although there are some examples which are discussed in Section 4.[43,44]

The band gap of n-type semiconducting single-crystal anatase $TiO_2$ is approximately 3.2 eV and the resistivity is $10^{15}$ $\Omega$ cm.[45] The lower edge of the CB is made up of vacant $Ti^{4+}$ 3d bands and the upper edge of the VB is made up of filled $O^{2-}$ 2p bands.[46] Bulk oxygen vacancies, titanium interstitials and reduced crystal surfaces generate shallow electron traps that can enhance the conductivity of $TiO_2$. Of particular interest here is the occurrence of $Ti^{3+}$ species, which form a band roughly 0.5 eV below the

Open Access Article. Published on 28 August 2015. Downloaded on 2/9/2026 4:13:16 PM. This article is licensed under a Creative Commons Attribution 3.0 Unported Licence.

$TiO_2$ CB. These defects act as n-type dopants, increasing the number of free electrons in the $TiO_2$ and hence the conductivity and current. At the same time defects can act as charge traps and are therefore recombination centers, having a negative effect on device performance.[45,47]

The number of defects can be influenced by moderately heating the device or by placing it in an inert atmosphere.[48] Furthermore, it was discovered that the number of traps can be reversibly changed by oxygen exposure or deprivation, indicating oxygen can adsorb onto $TiO_2$ defects and by doing so passivate trap states. A further remarkable observation is that UV irradiation causes the desorption of oxygen from these defects. Under exposure to air, oxygen release is counterbalanced by oxygen adsorption from the atmosphere. DSSCs are however typically protected from moisture and dye degradation by air-free encapsulation. The lack of oxygen inside the encapsulated device upsets the desorption–adsorption balance, leading to an increase in trap states and deterioration of device properties. This again is reversible upon breaking the seal and exposure to oxygen.[49–51]

Because of its many defects and the resulting sub-band gap states in $TiO_2$, electron transport is complex and hard to investigate. In devices, this is particularly difficult because parameters relating to one device property can not be studied individually without significantly changing other material properties. There is however strong theoretical and experimental evidence indicating that charge transport in $TiO_2$ proceeds by detrapping from sub-band gap states. These states lie deep in the tail of the density of states (DOS), from which electrons can be detrapped into the CB, according to the multiple-trapping model for charge transport.[8] The occupation of sub-band gap states at energy $E_A$ can be found through the Fermi–Dirac distribution function

$$F(E_A - E_{Fn}) = \frac{1}{1 + e^{(E_A - E_{Fn})/k_B T}} \tag{1}$$

and the density of carriers at the energy $E_A$ is $n_A = N_A F_A$, where $N_A$ is the total number of available trap sites at this energy. From this, the density of electrons in the CB ($n_{CB}$) can be derived as a function of the position of the quasi-Fermi level for electrons ($E_{Fn}$),

$$n_{CB} = N_{CB} e^{(E_{Fn} - E_{CB})/k_B T} \tag{2}$$

Considering electron transport takes place only in the CB, the conductivity of the film is given by

$$\sigma = n_{CB} e \mu, \tag{3}$$

where $\mu$ is the electron mobility. Generally, a higher $TiO_2$ conductivity means a higher current output from the device. From the equations above it is apparent that the conductivity of the film is determined by the probability of the electrons being in the CB, which increases as the quasi-Fermi level approaches the CB. This means that any modification that eliminates deep trap states will increase the conductivity of the film.[8]

To be able to effectively modify the trap states it is important to know where the traps are located. Different studies have suggested traps are located either in the bulk,[52] at inter-particle grain boundaries[53] or at the surface of the particles.[54,55] Bulk defects do not seem to play a major role[56] and it should be noted that charge recombination is an interfacial process.[57] But because of the difficulty to experimentally distinguish between boundary or surface defects it is still unclear were exactly the traps are located[8] and it can not be excluded that both traps at the grain boundaries and at the $TiO_2$ surface play an equally important role. Furthermore the synthesis method heavily affects defect locations and type. This makes it difficult to effectively modify the $TiO_2$ structure. It is understood that weakly reducing synthesis conditions and low annealing temperatures favor the formation of oxygen vacancies, whereas more reducing synthesis conditions and high annealing temperatures favor titanium interstitials as main defects.[26,45]

This combination of factors leads to the complex situation where shallow traps are essential for charge transport and can actually improve conductivity, but at the same time, deep traps lower the quasi-Fermi level and decrease conductivity. The voltage of the device, which is defined as the energy difference between the quasi-Fermi levels of $TiO_2$ and the HTM, is also affected by the trap states, with less deep traps resulting in a higher open circuit voltage. Furthermore, traps can act as recombination sites for electrons and holes,[26] which leads to a decrease in both current and voltage.

At the interface between $TiO_2$ and the HTM, band bending occurs due to the formation of a space charge region, implying that the CB in the bulk and at the surface do not have the same energy. The space charge region provides an electric field that separates electrons and holes. An external voltage can cancel out band bending and eliminate the space charge region. This specific voltage is called the flat-band potential $V_{FB}$.[58] Because trap states are predominantly located on the $TiO_2$ surface they have a large influence on $V_{FB}$ and thereby on the separation efficiency of electrons and holes. When $V_{FB}$ is negatively shifted (indicating an upward shift of the conduction band and the Fermi level), the injection of electrons from the dye into $TiO_2$ will become less efficient and a loss in current occurs. The reverse is also true and some defects make injection more efficient by positively shifting $V_{FB}$, causing a downward shift of the conduction band and Fermi level. With so many interconnected processes it is clear that devising a method to improve the electronic properties of $TiO_2$ is not trivial.

$TiO_2$ nanostructures for DSSCs can be synthesized in several ways, the most common methods discussed in this review are:

- *Sol–gel synthesis*. The sol–gel method is a versatile process that can be employed to make nanoparticles of ceramic materials. A colloidal suspension (sol) is made by hydrolyzing and polymerizing metal oxide precursors. The precursor typically is an inorganic metal salt or a metal organic compound. Frequently used precursors for $TiO_2$ are titanium tetrachloride ($TiCl_4$) and titanium isopropoxide (TTIP). When the polymerization is complete and the solvent has evaporated, the sol forms a gel. Heat treatment will transform the gel into the desired $TiO_2$ nanoparticle.[26]
- *Hydrothermal synthesis*. For the hydrothermal method a titanium precursor (TTIP) is mixed with water and a peptizer

Open Access Article. Published on 28 August 2015. Downloaded on 2/9/2026 4:13:16 PM. This article is licensed under a Creative Commons Attribution 3.0 Unported Licence.

($HNO_3$) after which the mixture is treated in an autoclave at elevated temperatures and pressures. After autoclaving the mixture is calcined to obtain $TiO_2$ nanoparticles.[26]

- *Solvothermal synthesis*. The solvothermal method is similar to the hydrothermal method, with the exception that the used solvent is non-aqueous. By choosing high boiling point solvents it is possible to achieve much higher temperatures, increasing the control over the particle formation.[26]
- *Flame spray pyrolysis*. For flame spray pyrolysis (FSP) titanium precursor is dissolved in a solvent to generate a source solution. This solution is vaporized using a spray nozzle onto a substrate which is kept at elevated temperatures (300–500 °C). During spraying the solvent evaporates due to the elevated temperature and nanoparticles are formed.[59]
- *Anodization*. $TiO_2$ nanotubes can be grown directly from titanium metal by applying a potential to a metal foil in a fluoride containing electrolyte solution. The tube length and diameter can be controlled through the anodization time and potential, electrolyte composition and pH. The amorphous nanotubes are then annealed at elevated temperatures to achieve crystalline $TiO_2$ nanotubes.[25,26,60]
- *Micelle method*. With the help of surfactants, micelles of $TiO_2$ precursor are formed in solution. Upon heat treatment these are converted to $TiO_2$ nanoparticles.[26]
- *Direct oxidation*. Titanium can be treated with oxidising agents to yield $TiO_2$ nanostructures,[61] similar to anodization.
- *Sonochemical synthesis*. Applying ultrasound to a solution can cause intense local heating, high pressures and enormous heating and cooling rates. This can be used to synthesize $TiO_2$ nanoparticles with high aspect ratios.[26,62]
- *Microwave synthesis*. Electromagnetic radiation can be used to heat up dielectrics to form nanostructures. A major advantage is the fast processing times due to the rapid heat transfer.[63]
- *Electrospinning*. An electrical charge is used to draw fibres from a solution, resulting in $TiO_2$ nanostructures with high aspect ratios.[64]

Compact $TiO_2$ films for electron blocking layers are synthesized through the following methods:

- *Spin coating*. A solution of $TiO_2$ precursor is spin coated on a substrate to form a thin layer of compact $TiO_2$.[65]
- *Spray pyrolysis*. This method is similar to that described for the synthesis of $TiO_2$ nanoparticles, with the exception that the particles form a dense layer on the substrate.[66]
- *Atomic layer deposition*. A substrate is alternatingly exposed to a $TiO_2$ precursor and $H_2O$, resulting in the deposition of atomically thick layers. The thickness of the layer can accurately be controlled through the number of cycles.[67]
- *Thermal oxidation*. A thin layer of titanium is deposited by sputtering or evaporation and subsequently heated to high temperatures in the presence of oxygen to oxidize the film which forms a compact $TiO_2$ layer.[68]
- *Electrochemical deposition*. A compact layer of $TiO_2$ can be deposited from a $TiO_2$ precursor solution by electrochemical deposition. The layer is subsequently crystallized by heating.[69]
- *Pulsed laser deposition*. For pulsed laser deposition a $TiO_2$ precursor is pressed to form a disk which is used as a laser target. The laser vaporizes the target and the vapor condenses on the substrate forming a thin layer.[70,71]

## 4 Doping

An effective way of modifying the electronic properties of $TiO_2$ is doping,[72] the deliberate insertion of impurities into the $TiO_2$-lattice. In silicon solar cells, doping is a frequently used method to improve conductivity. Here the effect can mainly be ascribed to the increase in free charges and thus conductivity, by the donation of electrons for dopants with a valency higher than that of the native material (n-type doping), or holes for dopants with a lower valency (p-type doping). In the case of $TiO_2$ the mechanism is much more complicated due to the defect ridden nature of $TiO_2$ and doping mainly affects the trap states and electronic structure of $TiO_2$, which is illustrated by the improvements that are made by doping with elements of equal valency as the host $TiO_2$ ions.[73] Doping can be achieved by either replacing the $Ti^{4+}$ cation or the $O^{2-}$ anion. Cationic dopants are typically metals, whereas anionic dopants are non-metals. Since the lower edge of the CB is made up of $Ti^{4+}$ 3d bands, replacing $Ti^{4+}$ by a different cation is thus expected to heavily affect the CB structure. The upper edge of the VB consists of $O^{2-}$ 2p bands and replacing $O^{2-}$ by a different anion affects the VB energy.

The atomic radius of the dopant should not differ much from the ion it replaces to prevent lattice distortion, introducing new defects that may hamper device performance.

Because dye molecules anchor to Ti atoms,[74] the replacement of Ti with another cation also affects dye adsorption due to different binding strengths between the dye and the dopant, or because the dopant induces oxygen vacancies.[75] Dopants often inhibit the growth rate of the $TiO_2$ nanoparticles, resulting in smaller particles.[76] This is in many cases beneficial since assemblies made from smaller particles have a larger surface area per volume of mesoporous $TiO_2$ compared to large particle assemblies. The increased surface area accommodates more dye, leading to higher light absorption and current densities. The main advantage of high light absorption is that thinner films can be used in photovoltaic devices, resulting in a reduction of recombination, which benefits both $J_{SC}$ and $V_{OC}$.

Morphology is a further factor that influences the properties of $TiO_2$. One-dimensional structures such as nanotubes have superior charge transport over nanoparticle assemblies, but have less surface area and thus adsorb less dye.[77] This implies that one-dimensional structures will benefit more from dopants that increase dye adsorption, whereas nanoparticle assemblies will benefit more from doping that leads to increased charge transport. The dopant source can also influence the effectiveness of doping and it has been shown that organic sources lead to better performances than inorganic salts.[78] Furthermore, doping influences the anatase to rutile phase transition.[79] The above factors complicate the study of the effect of doping on the electronic properties of $TiO_2$ as it is hard to distinguish and

Open Access Article. Published on 28 August 2015. Downloaded on 2/9/2026 4:13:16 PM. This article is licensed under a Creative Commons Attribution 3.0 Unported Licence.

quantify whether an improvement is caused by increased absorption or electronic effects.

The dopant can be introduced into the $TiO_2$-lattice in a number of ways:

- The most common method is simply mixing a dopant precursor with the $TiO_2$ precursor solution. This method can be employed in the sol–gel, hydrothermal, solvothermal, spray pyrolysis, atomic layer deposition, electrochemical deposition, sonochemical, microwave and electrospinning methods.[35]
- For pulsed laser deposition a dopant precursor is mixed with the titanium precursor and pressed to form a disk that can be used as a target for the laser.[70,71]
- By immersing the final $TiO_2$-structure into an electrolyte solution containing the dopant and applying a voltage to electrochemically dope the $TiO_2$.[80]
- For anodization and thermal oxidation, a Ti-dopant alloy can be used.[25,60]

The dopants can be grouped into separate categories that share common electronic configurations. These are (earth)alkali metals (Section 4.1), metalloids (Section 4.2), non-metals (Section 4.3), transition metals (Section 4.4), post-transition metals (Section 4.5) and lanthanides (Section 4.6).

In some cases co-doping with two or more dopants is applied to further increase device performance. Each dopant can separately enhance device properties.[81] One dopant can reinforce the effect of the other dopant,[82] or one dopant may counteract some of the detrimental effects caused by the other dopant.[83]

### 4.1 (Earth)alkali metals

The outer electron shell of the metals in this group consists of s electrons which can be easily donated,[84] making these metals interesting cationic dopants for $TiO_2$. The earth-alkali metals that have been used for $TiO_2$ doping are lithium,[85,86] magnesium[87–90] and calcium.[91–93]

**4.1.1 Lithium.** Using electrochemical impedance spectroscopy (EIS) and Hall effect measurements, it was found that $Li^+$-doping increases conductivity and charge densities in $TiO_2$, resulting in an increased $J_{SC}$. Fourier transform infrared (FTIR) spectroscopy indicated $Li^+$ is incorporated interstitially. It is suggested the observed $V_{OC}$ increase arises from a negative $V_{FB}$ shift, increasing $E_F$ and CB (Fig. 3b).[85]

To investigate the effect of particle size on doping, three different sized particles (22, 14 and 6 nm) were synthesized. In large particles bulk doping was dominant, while small particles exhibited mainly surface doping, as confirmed by X-ray diffraction (XRD). For the larger two particle sizes $Li^+$-doping decreased device efficiencies, while efficiencies increased for the smallest particle size. The loss in efficiency is ascribed to the formation of $Ti^{3+}$ species in the bulk that permanently trap electrons and decrease photocurrents. The enhanced efficiency for the smallest particle size is attributed to the $Li^+$ ions at the surface acting as temporary electron traps, which increases the electron lifetime and reduces recombination (EIS). $V_{OC}$ increases for all sizes caused by a band edge shift instigated by surface $Li^+$ adsorption.[86] The fact that doped small particles yield less efficient devices compared to undoped large particles (generally a decrease in particle size results in an increase in dye adsorption and efficiency) is an indication that several factors are playing a role, not only $Li^+$-doping. The large particles were obtained from commercial sources and contained substantial amounts of rutile, while the small particles were synthesized using a hydrothermal method and were pure anatase. This results in different $TiO_2$ particles that will not react similarly to doping.

In addition, $Li^+$ ions from the electrolyte can adsorb onto and intercalate into $TiO_2$, resulting in a positive shift of the CB (Fig. 3c) and reduced recombination.[94,95]

**4.1.2 Magnesium.** A high $V_{OC}$ of up to 1.2 V was reached by doping $TiO_2$ with $Mg^{2+}$.[87,88] A more detailed study showed $Mg^{2+}$ is introduced substitutionally and decreases particle size.

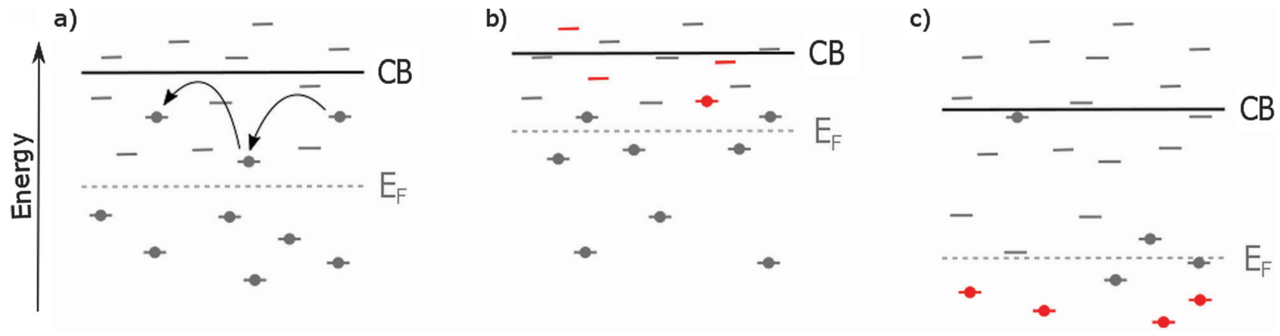

Fig. 3 The effect of $TiO_2$ doping on the CB and $E_F$. The doping induced states are shown in red. (a) In pristine $TiO_2$, electrons are transported by 'hopping' from shallow trap to shallow trap until they reach the electrode. The shallow trap density will thus influence electron transport rate and $J_{SC}$. Deep traps can permanently trap electrons and act as recombination sites, affecting $V_{OC}$. Another important factor determining $V_{OC}$ is $E_F$, as $V_{OC}$ is defined as the difference between $E_F$ of $TiO_2$ and the HTM. (b) Doping can decrease the deep trap density, resulting in an upward shift of $E_F$ and thus an increase of $V_{OC}$. The elimination of deep traps retards recombination and boosts the $V_{OC}$ even further. Because the CB is shifted towards the LUMO of the absorber, the driving force for electron injection is lowered, in combination with a decreased trap density and the related electron transport, lowering $J_{SC}$. (c) When doping contributes to the formation of deep traps, the conduction band and $E_F$ are shifted downwards. In combination with enhanced recombination through the deep trap states $V_{OC}$ decreases. Because of the larger offset between the CB and the absorber LUMO, electron injection is improved and the higher trap density causes an increase in electron transport, resulting in an enhanced $J_{SC}$. Ideally, the dopant eliminates deep traps while introducing new states close to CB, enhancing both $V_{OC}$ and $J_{SC}$ through decreased recombination and increased electron transport.

Open Access Article. Published on 28 August 2015. Downloaded on 2/9/2026 4:13:16 PM. This article is licensed under a Creative Commons Attribution 3.0 Unported Licence.

UV/Vis absorption spectroscopy showed a widening of the band gap indicating an upward shift of CB. This leads to an increase in $V_{OC}$, but because of decreased electron injection and lifetime $J_{SC}$ is reduced.[89]

Zn/Mg co-doped devices showed no effect on the optical band gap or $V_{OC}$. There is a positive shift in $V_{FB}$, indicating a lowering in $E_F$ and CB (Fig. 3c), and an increase in recombination sites, which might be compensated by faster electron transport. The faster transport, in combination with enhanced electron injection due to the shift of CB resulted in a marked increase in $J_{SC}$.[90]

**4.1.3 Calcium.** Doping $TiO_2$ with $Ca^{2+}$ was shown to drastically improve $J_{SC}$, but this was accompanied by a loss in $V_{OC}$. Mott–Schottky plots showed a positive shift of $V_{FB}$ (Fig. 3c) and an increased carrier density, which is associated with increased electron injection and higher $J_{SC}$, but at a loss in $V_{OC}$. Intensity-modulated photo current spectroscopy (IMPS) showed an increased electron mobility, which further increased $J_{SC}$.[91] Other studies showed similar increases in $J_{SC}$. By using a low doping concentration $V_{OC}$ was unaffected[92] or even improved by reducing the recombination rate.[93]

### 4.2 Metalloids

The elements that belong to the metalloid group have properties that lie between metals and non-metals, offering the possibility to combine the positive doping effects of metals and non-metals.[96] Metalloids regularly used for doping are boron,[97–100] silicon,[101] germanium[102] and antimony.[83,103]

**4.2.1 Boron.** Scanning electron microscopy (SEM) and XRD showed an increase in $TiO_2$ crystallinity upon $B^{3+}$-doping, which is beneficial for electron transport. X-ray photoelectron spectroscopy (XPS) indicated that $B^{3+}$ is incorporated both substitutionally and interstitially. Interstitial doping has been reported to be accompanied by a blue shift of the UV/Vis absorption spectrum[104] and an increase in oxygen vacancies,[105] which was confirmed by UV/Vis and electron paramagnetic resonance (EPR) spectroscopy. EIS showed an increase in electron recombination, which compensates the negatively shifted $V_{FB}$ (Fig. 3b) and leaves $V_{OC}$ unchanged. $J_{SC}$ is increased due to the increased electron transport.[97–99] Another study also reported improved crystallinity and interstitial doping for $TiO_2$ nanotubes. However, a red shifted absorption spectrum was also reported in this study and although recombination was retarded, a lower $V_{OC}$ was observed. A shift in $V_{FB}$ allowed for better charge injection, which in combination with improved crystallinity led to increased $J_{SC}$.[100]

**4.2.2 Silicon.** XRD showed increased crystallinity for $Si^{4+}$ doped $TiO_2$, which should have a positive effect on electron transport and recombination.[101]

**4.2.3 Germanium.** XRD and gas absorption surface area analysis (BET) indicate a decrease in particle size and an increase in surface area upon $Ge^{4+}$ doping of $TiO_2$, resulting in higher values of $J_{SC}$. $V_{FB}$ shows a negative shift (Fig. 3b), which results in an increase in $V_{OC}$.[102] Electron injection is probably reduced by this shift in $V_{FB}$, limiting $J_{SC}$.

**4.2.4 Antimony.** The introduction of $Sb^{3+}$ into $TiO_2$ did not affect the particle size, as measured by XRD. UV/Vis absorption spectroscopy showed a small decrease in band gap and $V_{FB}$ was shifted positively (Fig. 3c), resulting in a reduction of $V_{OC}$, which is in part compensated by reduced recombination. Despite a decrease in electron density and lifetime, the charge collection efficiency increased due to faster electron transport. Together with enhanced electron injection due to a lower $V_{FB}$, the faster electron transport resulted in increased $J_{SC}$.[103] This trend was confirmed by a second study, which also showed that the drop in $V_{OC}$ can be compensated by co-doping with $Cr^{3+}$, due to electron transfer from Sb to Cr, preventing the formation of oxygen vacancies and $Ti^{3+}$ species.[83]

### 4.3 Non-metals

Characteristic properties of non-metals are high ionization energies and high electro negativity. Because of these properties non-metals usually gain electrons when reacting with other compounds, forming covalent bonds. Among the non-metals are the only anionic dopants, which have a strong influence on the VB. Non-metal dopants are carbon,[99,106,107] nitrogen,[82,98,99,107–143] fluorine,[99,141,144–147] sulphur[82,118,120,128] and iodine.[148]

**4.3.1 Carbon.** Carbon was mainly incorporated interstitially, as measured by XPS, and resulted in a red shift in the UV/Vis spectrum. This is indicative of narrowing of the band gap, resulting in an increase in $J_{SC}$.[106] IMPS and intensity-modulated photovoltage spectroscopy (IMVS) showed increased transport rates and electron lifetimes, further contributing to increased values of $J_{SC}$ and $V_{OC}$.[99,107]

**4.3.2 Nitrogen.** Nitrogen doping usually causes a red shift of the absorption band edge[82,108–119] instigated by a positive shift of $V_{FB}$ (Fig. 3c), which improves electron injection.[120] Increased dye adsorption resulted in higher $J_{SC}$ values. XPS studies showed that $N^{3-}$ was introduced both substitutionally (replacing oxygen) and interstitially,[121] which was confirmed by EPR.[122] The introduction of $N^{3-}$ distorts the lattice and was reported to lower charge transport.[123,124] Most studies have however report increased charge transport rates[107,125–132] and/or longer lifetimes,[99,133–143] leading to an increase in $J_{SC}$ and $V_{OC}$.

Negative shifts in $V_{FB}$ (Fig. 3b) have been reported for Boron co-doped $TiO_2$, in combination with retarded recombination leading to a marked increase in $V_{OC}$.[98,99]

**4.3.3 Fluorine.** Fluorine-doping reduced the interfacial resistance between the $TiO_2$ blocking layer and FTO, significantly improving $J_{SC}$.[144] In mesoporous $TiO_2$ a decreased defect density was found, while crystallinity increased and the formation of brookite was inhibited. Improved crystallinity led to an increase in $J_{SC}$.[145] $I$–$V$ curves in the dark showed a decrease in parasitic resistances, leading to a marked increase in FF. EIS showed prolonged electron lifetimes, indicating that recombination was retarded, resulting in an increase in $V_{OC}$.[99,146,147] Co-doping with $Nb^{5+}$, $Sn^{4+}$, $Sb^{3+}$ or $Ta^{5+}$ resulted in a further increase in electron transport and decrease in recombination.[147] A positive shift of $V_{FB}$ (Fig. 3c) was reported to enhance electron injection while recombination was reduced.[141]

**4.3.4 Sulphur.** Sulphur is often used as a co-dopant for N-doping to further decrease the band gap energy and increase light absorption.[82,118,120,128]

Open Access Article. Published on 28 August 2015. Downloaded on 2/9/2026 4:13:16 PM.
This article is licensed under a Creative Commons Attribution 3.0 Unported Licence.

**4.3.5 Iodine.** Doping of $TiO_2$ with $I^{5+}$ can enhance light absorption and decrease recombination.[149,150] Dye adsorption studies showed that the amount of adsorbed dye is not significantly changed. UV/Vis spectroscopy showed a distinct absorption red shift upon doping, indicating a decrease in the band gap energy. This leads to more efficient electron injection and higher $J_{SC}$. EIS evidenced a decreased recombination rate, resulting in a higher $V_{OC}$.[148] DFT calculations predict that $I^{5+}$ doping can improve conductivity, $V_{OC}$ and light absorption.[151]

### 4.4 Transition metals

The incorporation of transition metals into $TiO_2$ gives rise to the formation of a wide range of new energy levels close to the CB arising from their partially filled d-orbitals. This makes transition metals suitable materials to tune the CB structure. The transition metals discussed here are scandium,[152] vanadium,[153–155] chromium,[83,156–159] manganese,[160–162] iron,[163,164] cobalt,[160,162] nickel,[165–167] copper,[162,168,169] zinc,[90,126,130,161,170–178] yttrium,[179–181] zirconium,[102,140,182–184] niobium,[44,60,70,71,102,154,185–191] molybdenum,[166] silver,[192] tantalum[43,59,154,193–197] and tungsten.[64,81,174,198–202]

**4.4.1 Scandium.** $Sc^{3+}$ is an interesting dopant because of its similar size compared to $Ti^{4+}$. It creates a 'solid solution', where $Sc^{3+}$ embedding gives rise to defect sites. Synchrotron scattering measurements showed substitutional incorporation of $Sc^{3+}$ with a minimal distortion of the $TiO_2$-lattice. BET and pore size and volume analysis (BJH) showed surface area and porosity were not affected in the relevant concentration range and dye adsorption was unchanged. $V_{FB}$ was shifted negatively (Fig. 3b), which was confirmed by widening of the band gap. This should result in a $V_{OC}$ increase, but lower $J_{SC}$ through reduction of electron injection. A lowering of $V_{OC}$ was however observed, possibly due to an increase in series resistance. Carrier density and transport rate decreased, but electron lifetime increased, resulting in an increase in $J_{SC}$.[152]

**4.4.2 Vanadium.** A gradient with decreasing $V^{5+}$ doping was generated by the sequential deposition of differently doped $TiO_2$ nanoparticles, which enhanced electron transport. A gradual red shift in UV/Vis absorption spectra with increasing doping concentration indicated a positive shift in $V_{FB}$ (Fig. 3c). In the used device architecture the layered structure formed a graded pathway along which electrons can be transferred to the electrode (Fig. 4). This led to an increase of the electron transfer rate and decreased recombination, leading to higher $J_{SC}$ and $V_{OC}$.[153] The $V_{FB}$ shift was also found in a different study through Mott–Schottky plots. IMPS and EIS showed an increase in transport rate which further enhanced $J_{SC}$.[154,155]

**4.4.3 Chromium.** $Cr^{3+}$ doping of $TiO_2$ led to a clear red shift in the UV/Vis absorption spectrum, evidencing a decrease in band gap and VB shift, which resulted in a slightly lower value of $V_{OC}$. Although dye adsorption is not affected, $Cr^{3+}$ doping seems to influence the $TiO_2$ crystal structure, as a clear rutile peak was detected in the XRD spectrum. EIS shows a decrease in charge transfer resistance and open-circuit voltage decay (OCVD), and an increase in electron lifetime, which led to higher values of $J_{SC}$. It was suggested that the reason for the better conductivity is an increase in free charges injected by $Cr^{3+}$ doping.[156]

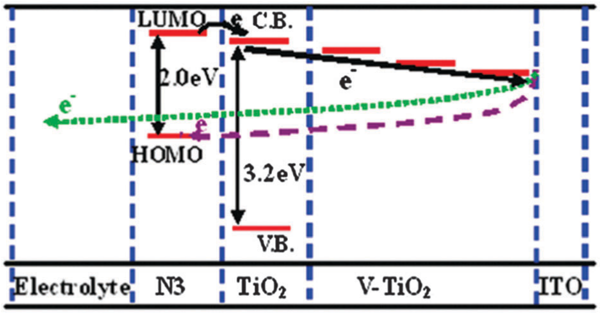

Fig. 4 Schematic diagram of the energy levels for V-doped $TiO_2$ DSSCs, showing the gradient induced by the different $V^{5+}$ doping levels. Reprinted with permission from ref. 153. Copyright 2011 American Chemical Society.

For the high $Cr^{3+}$ doping concentration of 3 at% rutile formation was inhibited, but some brookite formed instead, and the dye adsorption was increased. The optical band gap was decreased, increasing electron injection efficiency, at the expense of a $V_{OC}$ reduction.[157] The exact role of mixed crystal phases remains poorly understood.

At very high $Cr^{3+}$ doping concentrations of ∼10%, $TiO_2$ behaves as a p-type semiconductor, as confirmed by measuring the Hall effect. The introduction of $Cr^{3+}$ into $TiO_2$ causes $E_F$ to move towards the VB. This made it possible to construct a $TiO_2$ based p–n homojunction. Because of the diode like character, recombination is repressed, leading to an increase in $J_{SC}$ and efficiency.[158,159]

A high-throughput testing of dopants showed that Cr co-doped with Sb resulted in a massive increase in $J_{SC}$ and a small decrease in $V_{OC}$. It is suggested that this is caused by an electron transfer from Sb to Cr, which prevents the formation of oxygen vacancies and $Ti^{3+}$ species.[83]

**4.4.4 Manganese.** It was shown that $Mn^{2+}$ doping can reduce particle size (XRD) and increase surface area (BET), but because of a positive shift of $V_{FB}$ (Fig. 3c) and the introduction of a large number of recombination sites due to a high doping concentration, $V_{OC}$, $J_{SC}$ and efficiency decreased.[160] A separate study did not show a reduction in particle size. But because of the positive shift of $V_{FB}$, $J_{SC}$ was enhanced, resulting in a slightly higher efficiency.[161,162]

**4.4.5 Iron.** $Fe^{3+}$-doping was reported to reduce the trap density and charge recombination, while improving dye adsorption, resulting in drastically improved values of $J_{SC}$.[163]

At high concentrations (∼10%) of $Fe^{3+}$, $TiO_2$ behaves as a p-type semiconductor. The introduction of $Fe^{3+}$ into $TiO_2$ caused $E_F$ to move towards the VB. This made it possible to construct a $TiO_2$ based p–n homojunction. Because of the diode like character, recombination was reduced.[164]

**4.4.6 Cobalt.** Cobalt doping of $TiO_2$ was shown to drastically deteriorate DSSC performance due to the formation of sub-band gap states that reduce $V_{OC}$ and act as recombination centres, as evidenced by UV/Vis absorption spectroscopy and EIS.[160,162] The used doping concentration in ref. 160 was however rather high at 12.6 at%. Doping at these high concentrations is likely to give rise to massive lattice distortions and

Open Access Article. Published on 28 August 2015. Downloaded on 2/9/2026 4:13:16 PM. This article is licensed under a Creative Commons Attribution 3.0 Unported Licence.

accompanying defects. Low doping of 0.2 at% in ref. 162 showed a much more modest decrease in efficiency.

**4.4.7 Nickel.** $Ni^{2+}$-doping was shown to enhance the crystallinity of electrospun $TiO_2$ nanowires, enhancing charge mobility. A Mott–Schottky plot showed a negative shift of $V_{FB}$ (Fig. 3b), which in combination with reduced recombination leads to improved $V_{OC}$.[165]

Separate studies found that $Ni^{2+}$ doping decreased particle size, resulting in an increase in $J_{SC}$. The decreased band gap indicates a positive shift of $V_{FB}$ (Fig. 3c). The $V_{OC}$ loss was compensated by a reduced recombination rate.[166,167]

**4.4.8 Copper.** Surface doping of $TiO_2$ with $Cu^{2+}$ drastically increased both $J_{SC}$ and $V_{OC}$. The increase in $V_{OC}$ is caused by a negative shift of $V_{FB}$ (Fig. 3b) due to the interaction of $Cu^{2+}$ with defect states. OCVD showed that recombination was suppressed resulting in improved $J_{SC}$. $Cu^{2+}$ doping also seems to improve the electron transfer from the dye to the electron conductor by providing an alternative route for electrons from the dye into $TiO_2$.[168]

Other studies confirmed the negative shift of $V_{FB}$ and showed a similar increase in $V_{OC}$. Despite an increase in adsorption, $J_{SC}$ decreased drastically, caused by less efficient electron injection and a redox reaction of Cu with the electrolyte.[162,169]

**4.4.9 Zinc.** Because of the similar ion sizes of $Ti^{4+}$ and $Zn^{2+}$, lattice distortion is small when inserting $Zn^{2+}$ into the $TiO_2$-lattice, which was confirmed by XRD. $Zn^{2+}$-doping was shown to increase both $J_{SC}$ and $V_{OC}$.[170] $V_{FB}$ was negatively shifted (Fig. 3b), while recombination increased, resulting in a slight increase in $V_{OC}$. The electron density and transport rate were increased, leading to higher values of $J_{SC}$.[171,172] By reducing recombination and increasing surface area and dye adsorption a massive increase in efficiency could be achieved,[173,174] but the negative shift of $V_{FB}$ can lead to severely decreased electron injection and $J_{SC}$.[175]

In contrast, other studies reported a positively shifted $V_{FB}$ (Fig. 3c) and reduced recombination, while electron densities and transport were increased as well.[90,126,130,161,176,178] $Zn^{2+}$ doping was also shown to inhibit the anatase–rutile phase transformation, increasing device performance.[177]

The discrepancy in $V_{FB}$ shift can be explained by the close proximity of the CB of ZnO and $TiO_2$.[203] Slight variations in synthesis protocols might result in the $Zn^{2+}$ impurity energies being either below or above the CB of $TiO_2$, resulting in a positive or negative shift of $V_{FB}$ respectively.

**4.4.10 Yttrium.** Previous studies have shown that $Y^{3+}$-doping does not affect the optical band gap,[41] which suggests that $J_{SC}$ could be improved without suffering a loss in $V_{OC}$. Mott–Schottky plots showed that $Y^{3+}$-doping can negatively shift $V_{FB}$ (Fig. 3b) leading to improved values of $V_{OC}$. In addition $J_{SC}$ was significantly enhanced, which was attributed to up-conversion. Incident photon to current efficiency (IPCE) however showed an improvement for the entire optical spectrum which suggests additional effects play a role in improving $J_{SC}$.[179,180]

In another study the interstitial incorporation of $Y^{3+}$ into the $TiO_2$-lattice was confirmed by XRD. The surface area of mesoporous assemblies was slightly increased, increasing dye adsorption. Contrary to previous literature, UV/Vis absorption spectroscopy showed a marked decrease of the band gap and an increase in conductivity. Charge extraction measurements showed no change in trap density and the energy distribution below the CB. Photovoltage decay measurements showed an increase in electron lifetime, but this comes at a loss in the transport rate. The increase in $V_{OC}$ seems to be a result of a reduction in recombination, compensating the positive $V_{FB}$ shift (Fig. 3c). $J_{SC}$ increased due to better electron injection and collection efficiencies. In addition, no $TiCl_4$ treatment of the $TiO_2$ scaffold was needed simplifying device manufacture.[181]

**4.4.11 Zirconium.** The CB of $ZrO_2$ is located $\sim$0.7 eV above the CB of $TiO_2$. From this it can be expected that doping $TiO_2$ with $Zr^{4+}$ will shift the CB upwards.

$Zr^{4+}$-doping proved to decrease particle size, resulting in an increased surface area of nanoparticle assemblies and dye adsorption. The band gap was indeed found to be increased, indicating a negative shift of $V_{FB}$ (Fig. 3b). These factors contributed to increased values of $J_{SC}$ and $V_{OC}$.[182] Additional research found that the recombination rate was hardly affected and that the improved $V_{OC}$ was purely caused by the CB shift.[183] Other studies reported much higher,[102,184] or lower recombination rates upon doping.[140]

**4.4.12 Niobium.** Niobium is probably the most studied cationic dopant for $TiO_2$ in DSSCs because of promising optical and electronic properties.[204] Even for this well studied system, there are some discrepancies between different reports, which indicates that the effect of the doping is strongly dependent on the type of defects induced by the $TiO_2$ synthesis method.

Initial attempts were not very successful as a positive shift of $V_{FB}$ (Fig. 3c) and a decrease in dye adsorption led to poor device efficiencies,[102] although charge mobility was increased.[185]

In further studies a $Nb^{5+}$ doped HBL deposited *via* pulsed laser deposition showed an increase in $J_{SC}$, but a minute loss in $V_{OC}$. EIS showed slightly more current leakage for the doped compact layer, leading to a lower $V_{OC}$. But in addition the resistivity between the HBL and mesoporous $TiO_2$ dropped, leading to more efficient electron transfer between the two layers and thus a higher $J_{SC}$.[70] Optimization of the deposition protocol prevented leakage and led to an increase in $V_{OC}$.[71]

A novel water soluble $Nb^{5+}$-precursor made it possible to evenly distribute $Nb^{5+}$ ions throughout anatase $TiO_2$, resulting in more efficient devices. XRD showed an increase in crystallite size, but dye adsorption remained largely unchanged, indicating that the particle size was not affected. This means there are less grain boundaries in the material, or the particles were bigger and $Nb^{5+}$ increased the dye concentration,[205] improving in both cases the conductivity of the material. UV/Vis absorption showed a decreased band gap and positively shifted $V_{FB}$, resulting in more efficient electron injection at the expense of a lower $V_{OC}$. EIS confirmed the drop in resistivity between $TiO_2$ particles and showed that doping reduced recombination, in part compensating the loss in $V_{OC}$ by the shift of $V_{FB}$.[186] Another study showed a positive shift of $V_{FB}$ by a Mott–Schottky plot and an increased transport rate by IMPS,[154] resulting in a lower $V_{OC}$ but higher $J_{SC}$.

Open Access Article. Published on 28 August 2015. Downloaded on 2/9/2026 4:13:16 PM.
This article is licensed under a Creative Commons Attribution 3.0 Unported Licence.

A similar trend was found for devices doped with 2.5 mol% $Nb^{5+}$. Interestingly, $V_{OC}$ increased for these low concentrations, caused by a decrease of oxygen vacancies and recombination. As the doping concentration increases, the CB is lowered, enhancing electron injection and $J_{SC}$.[187] EIS showed an increase in electron lifetime at low concentrations, but for higher doping concentrations shorter electron lifetimes were observed. This explains the observed $V_{OC}$ trend. The transport rate was increased leading to a higher $J_{SC}$.[188] It was found that the drop in $V_{OC}$ could be prevented by adding a hole conductor co-adsorbant, which drastically decreased recombination.[189]

It also proved to be possible to prevent a loss in $V_{OC}$ by lowering the doping concentration (<0.5 mol%). Smaller particles and a larger surface area led to increased dye adsorption. Charge extraction measurements showed a downward shift of the trap states, lowering the CB and $V_{OC}$. Transient studies showed longer electron lifetimes, but a lower transport rate, resulting in an overall higher charge collection efficiency. Reduced recombination compensated for the loss in $V_{OC}$ due to the shifted CB, resulting in a device with better $J_{SC}$ and $V_{OC}$, drastically improving efficiency.[190] Similar electronic properties were found for $Nb^{5+}$ doped $TiO_2$ nanotubes[60] and rutile nanorods.[44]

A recent study showed an increase in both $J_{SC}$ and $V_{OC}$. A decrease in recombination was observed through EIS and transient photo current and is responsible for the improved $V_{OC}$.[191]

These results seem to suggest that it is only possible to improve $J_{SC}$ without negatively affecting $V_{OC}$ when the $TiO_2$ is relatively defect free. In low-defect $TiO_2$, a small amount of $Nb^{5+}$ is needed to passivate oxygen defects and reduce recombination. This implies that only few $Nb^{5+}$ sub-band gap states are formed and the effect of these states on $V_{OC}$ is compensated by a reduction in recombination, while they increase $J_{SC}$ by enhancing electron injection. For lower quality $TiO_2$ much higher doping concentrations are needed to reduce recombination and improve electron injection, resulting in more sub-band gap states, which lowers $V_{OC}$ more than can be compensated through recombination suppression.

**4.4.13 Molybdenum.** $Mo^{6+}$-doping proved to effectively decrease particle size (XRD) and band gap (UV/Vis absorption). Due to the increased surface area, an increase in $J_{SC}$ was observed. Although a $V_{OC}$ loss might be expected as a result of the smaller band gap, the reduced recombination rate resulted in a much enhanced $V_{OC}$.[166]

**4.4.14 Silver.** Calculations have predicted that doping with $Ag^{+}$ can heavily affect the optic and electronic properties of $TiO_2$.[206] XRD evidenced the inhibition of rutile formation. Reduced charge transfer resistance due to enhanced charge transport results in higher $J_{SC}$. Increased charge lifetime indicates recombination is suppressed, resulting in higher $V_{OC}$ (EIS).[192]

**4.4.15 Tantalum.** XRD showed particle size was not affected by incorporation of $Ta^{5+}$. $V_{FB}$ was shifted positively (Fig. 3c), resulting in a lower $V_{OC}$ but enhanced electron injection. The electron density and transport rate were also increased, leading to an improved $J_{SC}$.[154,193–195] Interestingly, the opposite behaviour was found for $Ta^{5+}$ doped rutile nanowires.[43] An explanation can be found in a different study where anodized $Ta^{5+}$-doped $TiO_2$ nanotubes were annealed at 450 °C and 550 °C, inducing different defects and mixtures of crystal phases. The devices annealed at 450 °C showed characteristics similar to ref. 193, whereas the devices annealed at 550 °C contained a larger fraction of rutile and characteristics were more similar to ref. 43 suggesting the difference is largely caused by the rutile content.[197] The CB of rutile has been reported to be approximately 0.2 V lower than the CB of anatase.[207] When $Ta^{5+}$ induces defects in this 0.2 V wide range it will have opposite effects on the electronic properties. This is probably also true for anatase $TiO_2$ that is synthesized by different methods and as a result has a different distribution of defect states, varying the position of CB.

Other studies found both $J_{SC}$ and $V_{OC}$ were increased, which was attributed to increased dye adsorption,[196] Mott–Schottky plots showed a negative shift of $V_{FB}$ (Fig. 3b). $V_{OC}$ was further enhanced by suppressed recombination (EIS, IMVS).[59,197]

**4.4.16 Tungsten.** XRD showed $W^{6+}$ insertion results in smaller particles and thus mesoporous assemblies with bigger surface areas. An increase in $J_{SC}$ was found, although dye adsorption was unchanged. The electron lifetime was greatly enhanced indicating a reduction in recombination.[81,174] A more detailed study shows a similar trend in device performance. $V_{FB}$ was shown to be positively shifted (Fig. 3c), improving electron injection but at the cost of lowering $V_{OC}$. IMPS showed a decrease in electron diffusion, IMVS an increase in electron lifetime and thus a decrease in recombination, compensating for the lower CB.[198] This was further confirmed by DFT calculations,[199] EIS[200,201] and OCVD.[202]

One study reported a blue shift of the absorption band edge (UV/Vis absorption) for electrospun nanowires, indicating a negative shift in $V_{FB}$ (Fig. 3b), which in combination with longer electron lifetimes led to a marked increase in $V_{OC}$. An increase in dye adsorption caused $J_{SC}$ to improve as well.[64]

### 4.5 Post-transition metals

In the periodic table the post-transition metals are located between the transition metals and the metalloids. As such, post-transition metals have some non-metal properties, showing covalent bonding effects. The investigated post-transition metals are aluminum,[51,80,81,208–210] gallium,[181] indium[83,211] and tin.[73,78,83,147]

**4.5.1 Aluminum.** Aluminum is a group III metal with good optical quality, low resistivity and high conductance.[212] This makes $Al^{3+}$ an interesting candidate for doping.

In $Al^{3+}$ doped $TiO_2$ improved values of $V_{OC}$ were reported, with largely unaffected $J_{SC}$. XPS studies showed a decrease in $Ti^{3+}$ defects, which was accompanied by a decrease in recombination. This resulted in a higher $V_{OC}$, but reduced $J_{SC}$. Higher dye loading in mesoporous $Al^{3+}$-doped $TiO_2$ compensated this loss and photo currents for doped and undoped samples were comparable.[81] The increase in $V_{OC}$ might also be caused by a negative shift of $V_{FB}$ (Fig. 3b) as was evidenced by UV/Vis absorption spectroscopy.[208] A decrease in the number of trap states was also shown by photo-thermal deflection spectroscopy (PDS).

Open Access Article. Published on 28 August 2015. Downloaded on 2/9/2026 4:13:16 PM. This article is licensed under a Creative Commons Attribution 3.0 Unported Licence.

Additionally it was shown that by decreasing the number of trap states the device is much less sensitive to UV instigated oxygen desorption, leading to significantly longer device lifetimes.[51] Another study found that $V_{FB}$ was slightly negatively shifted upon $Al^{3+}$-doping due to an increase in trap density, but this was compensated by an increase in current caused by longer electron lifetimes. XPS studies showed no change in the $Ti^{3+}$ concentration with $Al^{3+}$-doping. In this study there is no clear evidence that $Al^{3+}$ dopes into the $TiO_2$-lattice. It is more likely that islands of $Al_2O_3$ were formed on the $TiO_2$ surface, which may acts as a blocking layer, increasing electron lifetime.[80] For 20% $Al^{3+}$ doped $TiO_2$ it was found that $Al^{3+}$ substituted both into the $TiO_2$-lattice and formed a separate $Al_2O_3$ phase. Substitutional $Al^{3+}$ eliminated deep traps by substituting $Ti^{3+}$, resulting in a higher $V_{OC}$. A larger surface area of the mesoporous electrode and better charge injection resulted in a larger $J_{SC}$, while the $Al_2O_3$ phase acted as a blocking layer, preventing charge recombination.[209]

Al-doping was shown to inhibit the formation of rutile, leading to a decreased band gap and enhancing $J_{SC}$ through improved electron injection. A larger surface area of the nanoparticle assembly and higher anatase content further improved $J_{SC}$. Reduced recombination rate partially compensated the loss in $V_{OC}$ due to the band gap reduction.[210]

**4.5.2 Gallium.** Previous studies have shown that $Ga^{3+}$-doping does not affect the $TiO_2$ optical band gap,[213] which suggests that $J_{SC}$ can be improved without suffering a loss in $V_{OC}$.

The incorporation of $Ga^{3+}$ into the $TiO_2$-lattice was confirmed by XRD. A Rietveld analysis showed that $Ga^{3+}$ substitutes $Ti^{4+}$ in the $TiO_2$-lattice. The surface area and porosity of nanoporous electrodes were slightly increased, allowing an increase in dye adsorption. XPS showed an increase in oxygen vacancies upon $Ga^{3+}$-doping. Despite the increase in oxygen vacancies, a drop in resistivity was measured. Charge extraction measurements showed no change in the trap density and energy distribution below the CB. Photovoltage decay measurements showed an increase in electron lifetime, but this came at a loss in the transport rate. The increase in $V_{OC}$ seemed to be a result of a reduction in recombination, rather than a shift of the CB. In addition, no $TiCl_4$ treatment of the mesoporous scaffold was needed.[181]

**4.5.3 Indium.** Although most studies focus on the doping of the mesoporous $TiO_2$ structure, doping of the HBL can also lead to a marked increase in performance. It was shown that the transmittance of a $In^{3+}$-doped HBL was higher than that of pristine $TiO_2$. This allows more photons into the active layer, leading to an increase in absorption and $J_{SC}$. The observed negative shift in $V_{FB}$ (Fig. 3b) of the HBL will also result in a shift in $V_{FB}$ of the mesoporous $TiO_2$, leading to a higher $V_{OC}$. A decrease in dark current and a higher onset potential is an indication that the $In^{3+}$ doped HBL prevents recombination more effectively, which is supported by a longer electron lifetime as measured by EIS and OCVD. The $V_{FB}$ shift and reduced recombination led to a higher $V_{OC}$.[211]

A high throughput screening of 35 elements showed that $In^{3+}$ was one of the most promising dopants (along with Sb and Sn). This study similarly found a negative shift for $V_{FB}$.[83]

**4.5.4 Tin.** The particle size and dye adsorption were not affected by $Sn^{4+}$-doping. $V_{FB}$ was negatively shifted (Fig. 3b), resulting in an increase in $V_{OC}$, which was limited by increased recombination because the $Sn^{4+}$-ions acted as recombination centers. The increase in electron density and faster transport led to a higher electron collection efficiency and $J_{SC}$.[73,78,83,147]

### 4.6 Lanthanides

Because of their 4f bands, lanthanides provide interesting optic and electronic properties,[214] such as up-conversion, photoluminescence or down-conversion,[215,216] making it possible to harvest photons that are outside the absorption region of most dyes (400–800 nm). Although there are some reports that show effective up- or down-conversion,[216–218] these processes are not yet very efficient in DSCCs, and their exact role in improving device efficiencies is unclear. Because many optical conversion studies do not consider the effect of doping on the electron transport rate and lifetime, the exact contribution of conversion is hard to quantify. Lanthanides that have been used to dope $TiO_2$ are lanthanum,[219–221] cerium,[222,223] neodymium,[224] samarium,[225,226] europium,[225,227–230] erbium,[229,231–236] thulium[237,238] and ytterbium.[231,232,234–239]

**4.6.1 Lanthanum.** Lanthanum is an interesting element because of its high binding strength to oxygen. When $La^{3+}$ is doped into $TiO_2$, it will scavenge oxygen and induce vacancies on the surface.[240] XRD and BET analyses showed that the particle size and the mesoporous surface area were largely unaffected by doping, but the dye adsorption was significantly increased. This can be explained by an increase in oxygen vacancies, which has been reported to increase dye loading.[75] This theory has been confirmed by EPR analysis, which showed a strong correlation between density of oxygen vacancies, dye loading and device efficiency.[219,220]

A post-treatment with an acidic $La^{3+}$ solution was shown to drastically increase $J_{SC}$ although no $La^{3+}$ was detected in the final particles and no morphology change was observed. An increase in electron density, combined with a down-shifted CB and increased dye adsorption was responsible for the increase in $J_{SC}$.[221]

**4.6.2 Cerium.** It is known that Ce induces unoccupied 4f states just under the $TiO_2$ CB.[241] This may enlarge the driving force for electron injection from the dye into $TiO_2$.

The crystallite size and dye adsorption capability were not significantly changed upon doping. XPS showed that both $Ce^{3+}$ and $Ce^{4+}$ were present and the VB was unaffected. The UV/Vis absorption spectrum showed a red-shift, which indicated that Ce indeed induces unoccupied 4f states just under the $TiO_2$ CB. This was confirmed by cyclic voltammetry. Charge extraction and EIS measurements showed an increase in the electron density and capacitance due to enhanced electron injection, resulting in a higher $J_{SC}$, but caused a loss in $V_{OC}$.[222] A follow up study showed that the dopant acted solely as a surface trap state and therefore it was possible to counteract some of the adverse effects of Ce-doping by a $TiCl_4$ treatment.[223]

**4.6.3 Neodymium.** UV/Vis absorption spectroscopy indicated narrowing of the band gap upon $Nd^{3+}$-doping. This suggests a

Open Access Article. Published on 28 August 2015. Downloaded on 2/9/2026 4:13:16 PM.
This article is licensed under a Creative Commons Attribution 3.0 Unported Licence.

downward shift of the CB, which would explain the reduced $V_{OC}$. The amount of adsorbed dye was unaffected, but due to enhanced electron injection and reduced recombination, $J_{SC}$ saw a marked increase.[224]

**4.6.4 Samarium.** $Sm^{3+}$-doping decreased the anatase particle size and increased dye adsorption. In combination with down-conversion this led to an improved $J_{SC}$.[225] Another study showed an additional improvement in $V_{OC}$, which was suggested to be the result of p-type doping and recombination reduction.[226]

**4.6.5 Europium.** Due to the 4f bands of $Eu^{3+}$ it is possible to achieve down-conversion with $Eu^{3+}$ doped $TiO_2$.[218] A second important effect is a shift of the CB. It was found that dye adsorption increased upon doping. IPCE shows an absorption increase for the entire optical spectrum, with a new peak around 260 nm caused by down-conversion, leading to an increase in $J_{SC}$.[225,227] Other studies reported a negative shift of $V_{FB}$ (Fig. 3b), leading to a higher $V_{OC}$.[228–230]

**4.6.6 Erbium.** $Er^{3+}$ has energy bands inside the band gap of $TiO_2$ which are expected to promote up-conversion. An increase in $J_{SC}$ was found, which was attributed to up-conversion, but doping effects likely play a big role as the IPCE over the whole spectrum is increased (Fig. 5). $V_{OC}$ was increased due to a negative shift of $V_{FB}$ (Fig. 3b).[229,231–234] EIS showed a drop in resistivity, indicating an improvement in conductivity and reduced recombination, further contributing to enhanced values of $J_{SC}$ and $V_{OC}$.[235] The absorption edge was found to be red-shifted indicating a downward shift of CB, although this was probably caused by the fluorine co-dopant.[236]

**4.6.7 Thulium.** The observed up-conversion improved $J_{SC}$ and an increase in $V_{OC}$ suggested an upward shift of the CB.[237,238]

**4.6.8 Ytterbium.** No significant change in particle size was observed upon $Yb^{3+}$-doping. Dark current measurements show decreased recombination, which explains an increase in $V_{OC}$.[239]

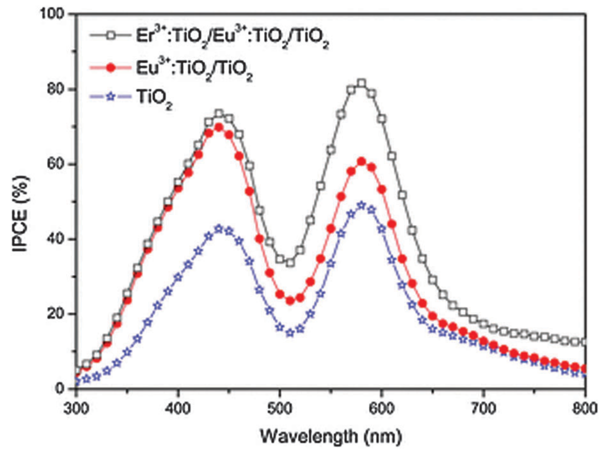

Fig. 5 IPCE of $Eu^{3+}$/$Er^{3+}$-doped $TiO_2$ DSSCs in light range of 300–800 nm. Although some of the increased IPCE above 700 nm can be ascribed to up-conversion, the drastic improvement for the whole spectrum suggests doping plays a more important role. Reprinted with permission from ref. 229. Copyright 2013 John Wiley & Sons, Inc.

Later studies report that due to up-conversion, $Yb^{3+}$ doping can enhance the $J_{SC}$. It was also suggested that the increased $V_{OC}$ was due to a negative $V_{FB}$ shift (Fig. 3b).[231,232,234–238]

### 4.7 Summary

In short, doping can affect five different properties of anatase $TiO_2$.

- *Flat-band potential*. $V_{FB}$ can be shifted either positively or negatively; a positive shift is indicative of a downward shift of the CB and $E_F$ while a negative $V_{FB}$ shift indicates an upward shift of CB and $E_F$. A positive shift of $V_{FB}$ makes electron injection easier, increasing $J_{SC}$. Because of a smaller difference between $E_F$ of $TiO_2$ and the HTM $V_{OC}$ is decreased. A negative shift of $V_{FB}$ will have the opposite effect on $J_{SC}$ and $V_{OC}$ (Fig. 3).
- *Recombination rate*. A decrease in the number of defect states usually enhances the electron lifetime and reduce recombination rate, resulting in an increase in $V_{OC}$. Because of the dependence on trap states for electron transport based on the trap-detrap mechanism, this can however lead to a decrease in electron mobility and $J_{SC}$.
- *Electron transport rate*. An increase in shallow trap states can lead to enhanced electron mobility and thus a higher $J_{SC}$. Simultaneously the introduced trap states can promote recombination which leads to a decreased $V_{OC}$ (Fig. 3).
- *Dye adsorption*. The dopant can change the growth rate of $TiO_2$ particles resulting in differently sized particles, affecting the amount of adsorbed dye and number of grain boundaries. Additionally, the dopant may affect dye adsorption by a change in binding affinity of the dye to the doped surface.
- *Phase transition*. Doping can inhibit the anatase-to-rutile phase transition, reducing rutile instigated charge recombination.

The main contributions for improving $TiO_2$ properties in DSSCs are summarized for each element in Table 1. This illustrates that the doping of $TiO_2$ with the aim to improve DSSC performance is not trivial. The correct balance between the CB energy, charge transport and recombination rate has to be found to obtain an optimally working device. It is important that the energy levels introduced by the dopant are located close to the CB to prevent these levels from becoming recombination centers or causing a large negative shift in $V_{FB}$, inhibiting charge injection. The best results are obtained for $TiO_2$ with few deep trap states. In this case, the properties of $TiO_2$ can be further improved by low-concentration doping, preventing the dopant from causing new trap states that give rise to detrimental effects such as increased recombination or decreased electron injection.

Because of the strong dependence of $TiO_2$ electronic properties on the fabrication protocol it is difficult to compare the effect of different dopants. This complicates the choice of dopant, particularly since opposite changes in device properties were found in many studies, employing the same dopant. For the moment, this means that for each synthesis method the ideal dopant and doping concentration has to be found by trial and error. High-throughput methods can be of significant help here, drastically cutting back the time needed to optimize each system.[83]

Open Access Article. Published on 28 August 2015. Downloaded on 2/9/2026 4:13:16 PM.
This article is licensed under a Creative Commons Attribution 3.0 Unported Licence.

Table 1 Dopants and their main contribution to the improvement of DSSCs

| Dopant | Comments | $V_{\mathrm{FB}}$ pos. | $V_{\mathrm{FB}}$ neg. | Recombination | Transport | Absorption |
|---|---|---|---|---|---|---|
| Lithium | | | 85 and 86 | 86 | 85 | |
| Magnesium | | | 89 | | | 89 |
| | Zn co-doped | 90 | | | 90 | |
| Calcium | | 91–93 | | 92 and 93 | 91–93 | |
| Boron | | | 97 | | 97 | |
| | Nanotubes | 100 | | 100 | 100 | |
| | N co-doped | | 98 and 99 | 98 and 99 | | |
| Silicon | | | | 101 | 101 | |
| Germanium | | | 102 | | | 102 |
| Antimony | | 103 | | | 103 | |
| | Cr co-doped | 83 | | 83 | 83 | |
| | F co-doped | | | 147 | 147 | |
| Carbon | | 99, 106 and 107 | | 99 and 107 | 99 and 107 | |
| Nitrogen | | 99 and 107–117<br>119 and 121<br>123–127<br>129–142 | | 133–143 | 107 and 125–127<br>129–132 | 108–117<br>119 and 121 |
| | S co-doped | 82 and 118<br>120 and 128 | | | | 82 and 118<br>120 and 128 |
| | B co-doped | | 98 and 99 | 98 and 99 | | |
| | Solid HTM | 122 | | | | 122 |
| Fluorine | | 141 | | 99 and 141<br>146 and 147 | 145 and 147 | |
| | Nb/Sn/Sb/Ta co-doped | | | 147 | 147 | |
| | Er co-doped | 236 | | | | |
| | HBL | | | | 144 | |
| Sulphur | N co-doped | 82 and 118<br>120 and 128 | | | | 82 and 118<br>120 and 128 |
| Iodine | | 148 | | 148 | | |
| Scandium | | | 152 | 152 | | |
| Vanadium | | 153–155 | | 153 | 153–155 | |
| Chromium | | 156 and 157 | | 156, 158 and 159 | 156 | 157 |
| | Sb co-doped | 83 | | 83 | 83 | |
| Manganese | | 161 and 162 | | | | 160 |
| Iron | | | | 163 and 164 | | 163 |
| Cobalt | Detrimental | | | | | |
| Nickel | | 166 and 167 | | 166 and 167 | | 166 and 167 |
| | Nanowires | | 165 | 165 | 165 | |
| Copper | | | 162, 168 and 169 | 168 | 168 | 162 and 169 |
| Zinc | | 126, 130 and 161<br>176 and 178 | 172–175 | 173 and 174 | 126 and 130<br>161 and 172<br>176 and 178 | 173, 174 and 177 |
| | N co-doped | | 171 | | 171 | |
| | Mg co-doped | 90 | | | 90 | |
| Yttrium | | 181 | | 181 | | 181 |
| | Co-doped | | 179 and 180 | | | 179 and 180 |
| Zirconium | | | 102 and 140<br>182–184 | 140 | | 182 |
| Niobium | | 154 and 186–188<br>189–191 | | 186 and 187<br>189–191 | 154 and 185–189<br>205 | 190 |
| | HBL | | | | 70 and 71 | |
| | Nanotubes | 60 | | 60 | | |
| | r-Nanorods | 44 | | 44 | | |
| Molybdenum | | 166 | | 166 | | 166 |
| Silver | | | | 192 | 192 | |
| Tantalum | | 154 and 193–195 | | | 154 and 193–195 | 196 |
| | FSP | | 59 | 59 | | |
| | Nanotubes | | 197 | 197 | | |
| | r-Nanowires | | 43 | 43 | | |
| Tungsten | | 198 | | 81, 174 and 198<br>200–202 | | |
| | Nanowires | | 64 | 64 | | 64 |
| Aluminum | | | 80, 208 and 209 | 80, 81 and 209 | | 81 and 209 |
| | Phase stab. | 210 | | 210 | | |
| | Solid | | 51 | | 51 | |
| Gallium | | | | 181 | | 181 |
| Indium | | | 83 | | | |
| | HBL | | 211 | 211 | | 211 |
| Tin | | | 73, 78 and 83 | | 73, 78 and 83 | |
| | F co-doped | | | 147 | 147 | |

This journal is © The Royal Society of Chemistry 2015

Open Access Article. Published on 28 August 2015. Downloaded on 2/9/2026 4:13:16 PM.
This article is licensed under a Creative Commons Attribution 3.0 Unported Licence.

Table 1 (*continued*)

| Dopant | Comments | $V_{FB}$ pos. | $V_{FB}$ neg. | Recombination | Transport | Absorption |
|---|---|---|---|---|---|---|
| Lanthanum | | 221 | | | | 219–221 |
| Cerium | | | | | 222 and 223 | |
| Neodymium | | 224 | | 224 | | |
| Samarium | | | | 226 | | 225 and 226 |
| Europium | | | 228–230 | | | 225 and 227–230 |
| Erbium | | | 229 and 231–234 | 235 | | 229 and 231–234 |
| | F co-doped | 236 | | | | |
| Thulium | | | 237 and 238 | | | 237 and 238 |
| Ytterbium | | | 231 and 232<br>234–238 | 239 | | 231 and 232<br>234–238 |

# 5 Outlook: perovskite solar cells

With the recent emergence of perovskite solar cells (PSCs) it will be interesting to see which lessons can be learned from DSSCs. Due to the high optical density and charge transport of perovskites, much thinner devices can be constructed and the influence of $TiO_2$ surface area is much reduced. Because of the instability of perovskite in liquid electrolytes[22] only solid HTMs are used. The high charge transport through the perovskite allows the construction of devices without mesoporous layer,[11] but it is presently difficult to produce pinhole free films,[242] limiting device performance. Mesoporous structures help wetting of the substrate and prevent the formation of pinholes.[12,13] Similar to DSSCs, most PSCs rely on a hole blocking layer of $TiO_2$.[10] This implies that the electronic properties of $TiO_2$ are also important, both as compact and mesoporous layers, and similar to dye-sensitised solar cells doping will be important for performance enhancements in PSCs. So far, Mg,[243] Nb,[244,245] Y,[246,247] Al[51] and Zr[248] doping of $TiO_2$ have been employed in perovskite solar cells.

Similar to Mg-doping in DSSCs,[87–89] $V_{OC}$ was improved in PSCs with a Mg-doped HBL, due to a higher CB energy and reduced recombination.[243] Nb-doping resulted in improved electron injection and transport, resulting in higher $J_{SC}$.[244,245]

In the case of Y-doping a small negative shift of $V_{FB}$ was observed and recombination is slightly reduced. The main reason for the improvement in device performance was increased perovskite loading, leading to a marked increase in $J_{SC}$.[246] A separate study found increased electron transport led to higher $J_{SC}$ for a planar device with doped HBL.[247]

Al-doping was shown to reduce the number of oxygen vacancies and the associated deep trap states, effectively reducing recombination and increasing conductivity of the film. This led to an overall increase in $J_{SC}$. Additionally, it was shown that the long-term stability in inert atmosphere was significantly enhanced. This was ascribed to the elimination of oxygen defects by Al-doping. UV radiation causes the desorption of oxygen and in an inert atmosphere, where adsorbed oxygen can not be replenished, this leads to the emergence of oxygen vacancies that act as deep trap states, deteriorating device performance (Fig. 6). By reducing the number of traps through Al-doping this deterioration effect is much less profound.[51]

A major problem in PSCs is hysteresis; the performance of the device depends strongly on how the measurement is performed. Typically the performance is much better sweeping from high to low voltages (forward bias) than *vice versa*, making it difficult to define the true power conversion efficiency. The precise mechanism causing hysteresis is yet unknown, although there are several hypotheses on the origin of hysteresis, such as the ferroelectric polarization,[21,249,250] ion migration[21,251] or deep trap states.[21] Trap states at the interface of perovskite and charge conducting material may play an important role. These trap states get filled under forward bias measurements, resulting in good contacts and high efficiency devices. Under short-circuit conditions the traps may empty, resulting in a poor device performance until the trap states are filled again.[21,251–255] It was shown that by passivating interfacial traps, hysteresis could be drastically reduced, while overall device performance was improved.[256] By doping $TiO_2$ with $Zr^{4+}$ hysteresis was decreased, while at the same time the CB was shifted upward and recombination was decreased, leading to an increase in $V_{OC}$.[248] This result suggests that doping can play an important role by decreasing surface trap states and reducing hysteresis.

Overall, it is likely that doping of $TiO_2$ may play an important role in improving efficiencies of PSCs. Doping can shift the CB, increase charge transport and reduce recombination. In addition, it may prolong device lifetimes, increase perovskite loading and play an important role in reducing hysteresis.

# 6 Techniques

There are several techniques that can give information on the effects of doping on the structural and electronic properties of $TiO_2$. This section discusses the most common techniques and the information that can be extracted from the measurements.

## 6.1 Computational modelling

Computational modelling can be used to predict and design material properties. Density functional theory (DFT) has become a popular method due to its low computational cost, making it possible to quickly screen dopants for their suitability to increase $TiO_2$ properties.[151,199] However, caution must be taken as the band gap is often underestimated, leading to inaccurate predictions.[257]

## 6.2 Morphological studies

To gain insight in the structure of (doped) $TiO_2$ several techniques can be employed. Electron microscopy offers the possibility to image nanostructures, from X-ray diffraction average particle size

Open Access Article. Published on 28 August 2015. Downloaded on 2/9/2026 4:13:16 PM.
This article is licensed under a Creative Commons Attribution 3.0 Unported Licence.

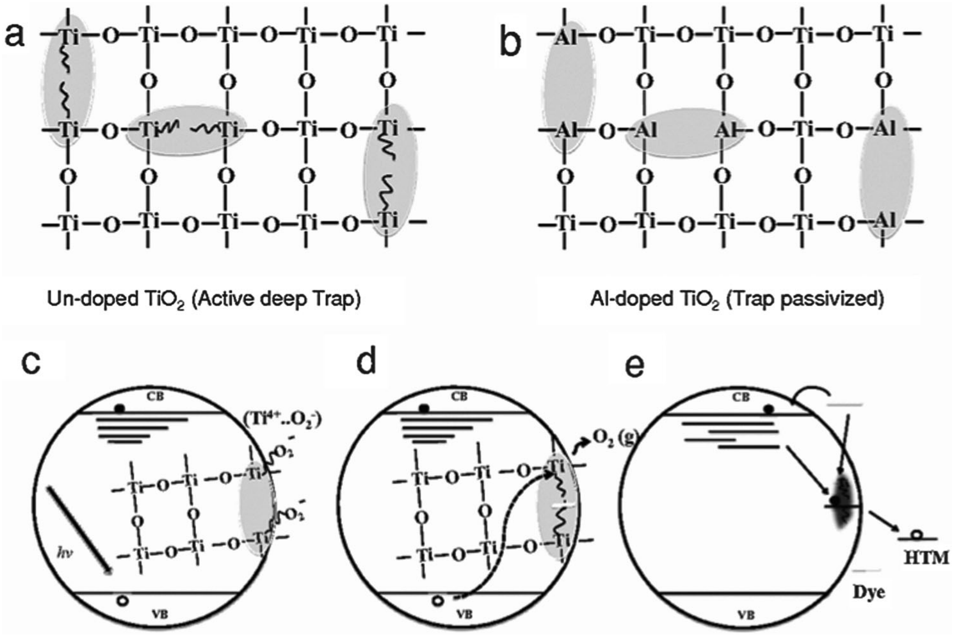

Fig. 6 Schematic of Ti(III) trap passivation, doping and oxygen adsorption. (a) Oxygen defects in the lattice give rise to Ti(III) defects that form deep electronic traps. (b) Al substitution at the Ti(III) sites passivates these defects. (c) In the presence of oxygen, ionisation of Ti(III) gives rise to $O^2$ superoxide which passivates the trap sites. (d) Photoexcited holes neutralise and desorb O2, activating Ti(III), which (e) enables charge recombination. Reprinted with permission from ref. 51. Copyright 2014 John Wiley & Sons, Inc.

and dopant distribution can be determined and surface analysis quantifies the effect of doping on surface area and dye adsorption.

**6.2.1 Electron microscopy.** Electron microscopy makes it possible to visualize and characterize nanostructures. Scanning electron microscopy (SEM) is generally used to study the surface topography and to measure the average particle size and film thickness. The latter can also be measured by a profilometer. If equipped with an energy dispersive X-ray (EDX) spectrometer, the distribution of elements in the film can also be mapped. Transmission electron microscopy (TEM) yields a higher resolution than SEM, but requires extremely thin samples, which makes TEM less well suited for topographic investigations. Atomic resolution allows to image the $TiO_2$ lattice and typically gives a better measurement of the average crystallite size.

**6.2.2 X-ray diffraction.** X-ray diffraction (XRD) is a precise method to determine the crystal structure of $TiO_2$. It is routinely used to determine the crystal structure and the presence of impurity phases. A typical XRD spectrum of anatase $TiO_2$ is shown in Fig. 7 with the Miller indices (*hkl*) of the different peaks. The Rietveld refinement method allows a more detailed analysis of XRD spectra by using a least squares fit to approximate the measured profile.[258] This way it is possible to determine the average crystallite size $D$ by using the Scherrer formula[259,260]

$$D = \frac{K\lambda}{\beta\cos\theta}, \tag{4}$$

where $K$ is a dimensionless shape factor which is dependent on the shape of the particle (0.9 for spherical particles), $\lambda$ is the wavelength of the X-rays, $\beta$ is the full width half-maximum (FWHM) after subtracting the instrumental line broadening and $\theta$ is the Bragg angle. It is important to note that $\beta$ and $\theta$ are in radians, whereas the instrumental output is usually in degrees. Furthermore, the inter-planar spacing $d_{hkl}$ can be calculated with Bragg's law[261]

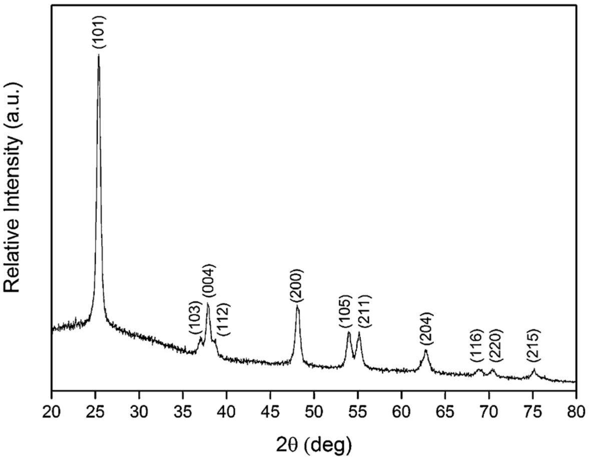

Fig. 7 X-ray diffraction spectrum of anatase $TiO_2$. Each peak is labeled with the corresponding Miller indices (*hkl*).

$$d = \frac{\lambda}{2\sin\theta} \tag{5}$$

and using this interplanar spacing the lattice parameters $a$ and $c$ can be calculated using the Bragg formula for a tetragonal ($a = b$) lattice[162]

$$\frac{1}{d^2} = \frac{h^2 + k^2}{a^2} + \frac{l^2}{c^2}. \tag{6}$$

Open Access Article. Published on 28 August 2015. Downloaded on 2/9/2026 4:13:16 PM.
This article is licensed under a Creative Commons Attribution 3.0 Unported Licence.

The change of the individual lattice parameters on doping can be determined by calculating the distortion degree of the lattice using[262]

$$R = \frac{2a\sqrt{2/3}}{c}. \tag{7}$$

Vegard's law provides an empirical method to assess the successful incorporation of a dopant. It states that there is a linear relation between the lattice distortion and the concentration of dopant. It requires that the crystal retains it lattice structure and the dopant and matrix form a solid solution.[263]

**6.2.3 Dye adsorption.** The amount of dye adsorbed on the $TiO_2$ surface is typically a good measure to determine how many photons will be absorbed. Dye adsorption depends on the porosity of the mesoporous $TiO_2$, which can be measured by gas adsorption. Gas adsorption isotherms are typically analyzed by the Brunauer–Emmett–Teller (BET) theory[264] that yields the specific surface area of the material or by the Barrett–Joyner–Halenda (BJH)[265] analysis, which yields the pore size distribution. Doping however often affects the adsorption of the dye to $TiO_2$ (*i.e.* the dye affinity) implying differing the amounts of adsorbed dye for samples with the same surface area. In a more direct measurement, the dye can be desorbed from $TiO_2$ using a non-reactive solvent. By comparing the UV-vis absorption of the extracted solvent to reference spectra, the amount of adsorbed dye can be estimated. A combination of the two methods can be used to calculate the average dye density.

### 6.3 Spectroscopic techniques

By studying the interaction between light and matter the electronic structure of the material can be determined. The band gap, presence of defect states and material composition can be found through these methods.

**6.3.1 UV/Vis spectroscopy.** The main use for UV/Vis spectroscopy in $TiO_2$ doping studies is to obtain the direct and indirect band gap by determining the position of the absorption band edge. Absorption and reflectance are recorded in the range of 300–800 nm. Absorption and the direct band gap $E_g$ are related through[266]

$$\alpha E = C(E - E_g)^{1/2}, \tag{8}$$

where $\alpha$ is the absorption coefficient, $E$ the photon energy and $C$ a proportionality constant. Sample reflectance can be converted to the Kubelka–Munk function,[267] which is equivalent to the absorption coefficient in eqn (8)

$$F(R) = \frac{(1 - R)^2}{2R}. \tag{9}$$

Using a Tauc plot (Fig. 8)[89,268] it is possible to extract the direct and indirect band gap. In a Tauc plot $(F(R)E)^{1/r}$ is plotted *versus* $E$, where $r = \frac{1}{2}$ for the direct band gap and $r = 2$ for the indirect band gap. Extrapolation of the linear regime gives the band gap energy.

**6.3.2 X-ray photoelectron spectroscopy.** In X-ray photoelectron spectroscopy (XPS) the sample is irradiated with X-rays and the number of escaping electrons and their energy are measured to gain information about the elemental composition and electronic state of the elements. For example, it is possible to quantify the amount of dopant in the sample and the $Ti^{3+}$ to $Ti^{4+}$ ratio.[81]

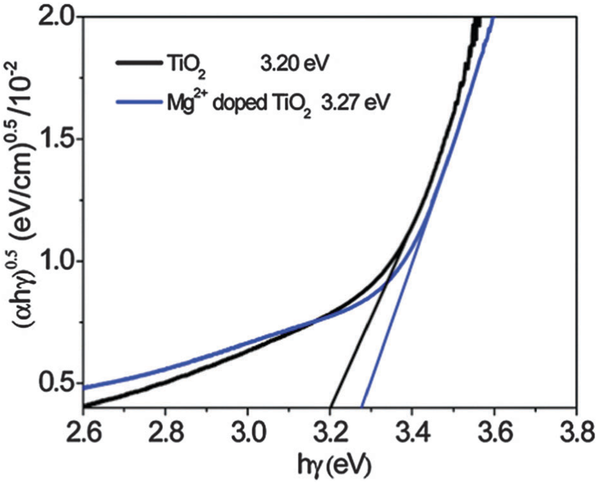

Fig. 8 Determination of the indirect band gap energy for a $TiO_2$ film and a $Mg^{2+}$-doped $TiO_2$ film from the plot of $(\alpha E)^{\frac{1}{2}}$ *versus* the excitation energy, $h\gamma$ ($\alpha$ is the absorption coefficient, $E$ is $h\gamma$, $h$ is Plancks constant, and $\gamma$ is the photon frequency). The indirect band gap energy is given by the intersect of the extrapolated linear regime with the $x$-axis. Reprinted with permission from ref. 89. Copyright 2011 American Chemical Society.

**6.3.3 FTIR spectroscopy.** Fourier transform infrared (FTIR) spectroscopy measures optical absorption in a wide spectral range (4400–4000 $cm^{-1}$) and gives information about atomic bond vibrations. The intensity and position of the peaks of stretching vibrations of Ti–O–Ti and Ti–O bonds give information about the interaction between $TiO_2$ and the dopant since they are related to the number and strength of Ti–O bonds. By doping into interstitial sites the dopant directly decreases the number of Ti–O bonds. The size, electron affinity and valency of the dopant also influences the strength and orientation of neighbouring Ti–O bonds.

**6.3.4 Raman spectroscopy.** Raman spectroscopy is used to find rotational, vibrational and other low-frequency modes in a system. A laser beam interacts with the samples modes, resulting in an up- or down-shift of the photon energy. Each material has a distinct spectrum which allows the identification of impurity phases. Dopants alter the modes and in this way it is possible to measure the effect of the dopant on the $TiO_2$ crystal lattice. Raman spectroscopy is particularly useful to detect the formation of oxygen vacancies.[269]

**6.3.5 Material composition.** Several methods are able to determine the amount of dopant in $TiO_2$ with great precision such as EDX spectroscopy,[169] XPS spectroscopy,[81] mass spectroscopy[187] or neutron activation analysis,[270] which make use of unique "fingerprint" measurement spectra obtained upon sample irradiation.

### 6.4 Electromagnetic measurements

The interaction between magnetic fields and free charges in the sample makes it possible to determine the type of conduction, carrier concentration and detect trap states.

Open Access Article. Published on 28 August 2015. Downloaded on 2/9/2026 4:13:16 PM. This article is licensed under a Creative Commons Attribution 3.0 Unported Licence.

**6.4.1 Hall effect measurement.** When a magnetic field is applied on a current-carrying semiconductor, the charge carriers experience a force perpendicular to the magnetic field and the current. This is called the Hall effect, by measuring the strength of this effect the type of conduction (p- or n-type) and the carrier concentration are determined.[271,272]

**6.4.2 Electron paramagnetic resonance analysis.** In electron paramagnetic resonance analysis (EPR) the spins of unpaired electrons are excited by microwave radiation in a magnetic field. This makes it possible to detect trapped electrons, which are unpaired, and the corresponding trap states.[220,273] The technique is similar to nuclear magnetic resonance analysis (NMR) with the exception that in NMR nuclear spins are excited.

### 6.5 (Photo-)electrochemical measurements

By simulating real world conditions the performance of the solar cell can be predicted through the determination of the photovoltaic properties such as short circuit current density $J_{SC}$, open circuit voltage $V_{OC}$ and fill factor FF.

A wide range of measurements where the sample is subjected to periodic optical or electronic perturbations provide information about the concentration, diffusion length and lifetime of electrons, CB position, density of trap states as well as transport and recombination processes. They include transient and decay measurements, electrochemical impedance spectroscopy (EIS), intensity modulated photo current spectroscopy (IMPS), intensity modulated photovoltage spectroscopy (IMVS) and open circuit voltage decay (OCVD).[9,274]

**6.5.1 Photovoltaic properties.** The power conversion efficiency of a solar cell is determined by measuring the current density as a function of applied voltage characteristics under illumination. The illumination spectrum and intensity should approximate that of the sun. To this end, a standardized light source of 100 mW cm$^{-2}$ AM 1.5 solar simulator is used. From the photo current–voltage (*I–V*) curve (Fig. 9) $J_{SC}$, $V_{OC}$ and FF are extracted. $J_{SC}$ is the current in the absence of a net voltage, $V_{OC}$ is the voltage in the absence of net current and FF is a measure for the "squareness" of the curve and is a good indication for the resistances in the device. FF is determined by dividing the maximum power output $P_{max}$ of the device by $J_{SC} \times V_{OC}$. Parasitic resistances in the device lower FF; for low voltages shunt resistances are dominating, while for high voltages the series resistance is important. These are revealed by *I–V* curves measured in the dark. Under dark conditions, a solar cell behaves as an ideal diode, and deviations from the ideal diode behaviour arise from injected current leakage.

The quantum efficiency is defined as the ratio of incident photons of a certain energy to the charges collected. The external quantum efficiency (EQE) considers all the incident photons including those that are transmitted and reflected, whereas internal quantum efficiency (IQE) only takes the absorbed photons into account. From this, a correlation between the energy of the photon and the probability of charge collection can be found.

Lastly, the stability of the device can be tested by measuring the device efficiency over a long period of time.

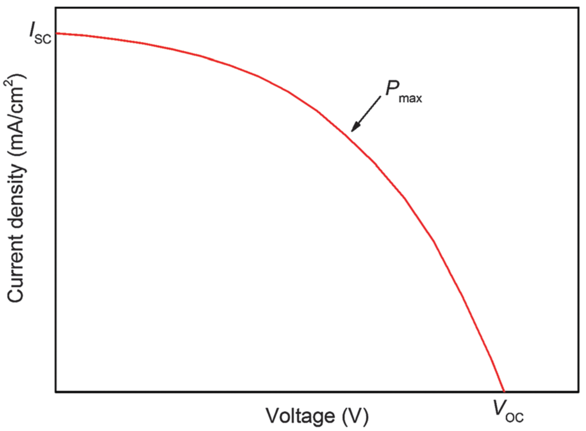

Fig. 9 Typical *I–V* curve for DSSCs. Short circuit current density $J_{SC}$ is given by the intersect with the *y*-axis and open circuit voltage $V_{OC}$ by the intersect with the *x*-axis. Fill factor FF can be calculated from $\frac{P_{max}}{J_{SC} \times V_{OC}}$.

**6.5.2 Electrochemical impedance spectroscopy.** By perturbing an applied voltage with a small sine wave modulation the impedance can be found through the sinusoidal current response. Impedance can be defined as the frequency domain ratio of the voltage with respect to the current and is a complex value. The resulting function can be visualised with a Nyquist plot, where the real part of the function is plotted on the *x*-axis and the imaginary part on the *y*-axis. The system can be described by an equivalent circuit consisting of parallel and series connected elements (Fig. 10). From this charge transfer and transport processes and capacitance can be extracted.[9,274,275]

**6.5.3 Electron transport.** Because electron transport and recombination processes respond non-linearly to different light intensities they can be studied using a small perturbation of light modulated onto a higher constant light intensity. The output can again be visualised with a Nyquist plot. In IMPS a sinusoidal modulation of light intensity is applied and the photo current is measured as a function of this modulation.[276]

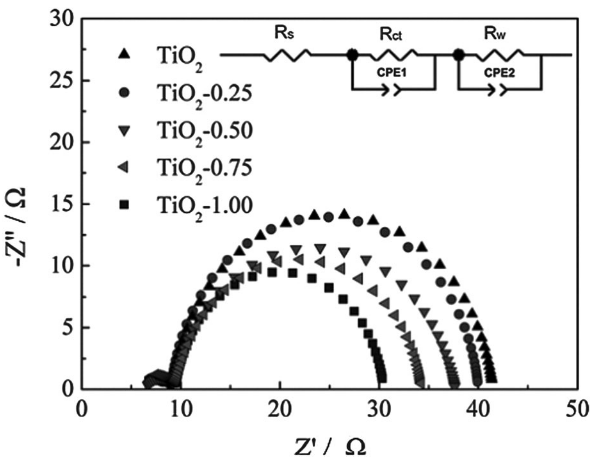

Fig. 10 EIS spectra of $TiO_2$ and Sn-doped $TiO_2$ DSSCs. The inset shows the equivalent circuit that was used to find the electron lifetime and capacitance. Reprinted with permission from ref. 73. Copyright 2012 American Chemical Society.

Open Access Article. Published on 28 August 2015. Downloaded on 2/9/2026 4:13:16 PM. This article is licensed under a Creative Commons Attribution 3.0 Unported Licence.

The photo current response $\tau_{pc}$ depends on both the electron transport and recombination.[54] Under short-circuit conditions, the electron lifetime $\tau_n$ is usually much larger than the transport time $\tau_{tr}$, implying $\tau_{pc} \approx \tau_{tr}$.[9]

The chemical diffusion coefficient $D_n$ can be derived from the transport time

$$D_n = \frac{d^2}{C\tau_{tr}}, \tag{10}$$

where $d$ is the thickness of the $TiO_2$ layer and $C$ is a constant which depends on the absorption coefficient and direction of illumination.[277]

**6.5.4 Electron lifetime.** The measurement of the electron lifetime is similar to the electron transport, but the open circuit potential rather than the photo current is measured. Under these conditions, photo-generated electrons are not extracted and will eventually recombine with holes. Using a small intensity modulation, the response time of the potential corresponds to the electron lifetime $\tau_n$.[278]

An alternative is the OCVD method, where $V_{OC}$ is measured as a function of time after the light source is switched off.[279] The electron lifetime is calculated from the slope of the transient as

$$\tau_n = -\frac{kT}{e}\left(\frac{dV_{OC}}{dt}\right)^{-1}. \tag{11}$$

The advantage of this method is that the electron lifetime can be determined for a wide potential range in just one measurement.

A third method is time-dependent charge extraction,[280] where the lifetime is given by

$$\tau_n = Q(t)\left(\frac{dQ(t)}{dt}\right)^{-1}. \tag{12}$$

$Q(t)$ is the extracted charge after decay in the dark for the time $t$, assuming recombination follows first-order kinetics.

IMVS and OCVD give similar values, while charge extraction usually gives a value that is about 4 times higher.[280] This can be explained by the fact that the former methods are based on the recombination of photo induced excess charges, whereas the latter method gives an average lifetime for all the electrons in the $TiO_2$.[9]

**6.5.5 Electron concentration.** The electron concentration can be measured through charge extraction methods, where the current is integrated over time after the light has been switched off.[281]

Alternatively the capacity is measured.[282] An open-circuit potential is established by a bias illumination after which a light pulse is applied. The resulting voltage rise is measured, while the transient photo current is measured separately under short-circuit conditions to calculate the injected charge. The capacity is given by the ratio of injected charge and voltage change.

Lastly, the electron concentration can be estimated from the slope of a Mott–Schottky plot (Section 6.5.6).

**6.5.6 Flat-band potential.** The flat-band potential $V_{FB}$ can be derived from a Mott–Schottky plot, where the capacitance of the space charge region is measured as a function of voltage under depletion conditions. For a fit of the linear part of the curve, $V_{FB}$ and electron density are given by the axis-intersect and the slope of the fit respectively (Fig. 11).[193,283] The flat-band potential is usually referenced to a standardized electrode. A negative shift is indicative of an upward shift of CB, whereas a positive shift indicates a downward shift of CB.

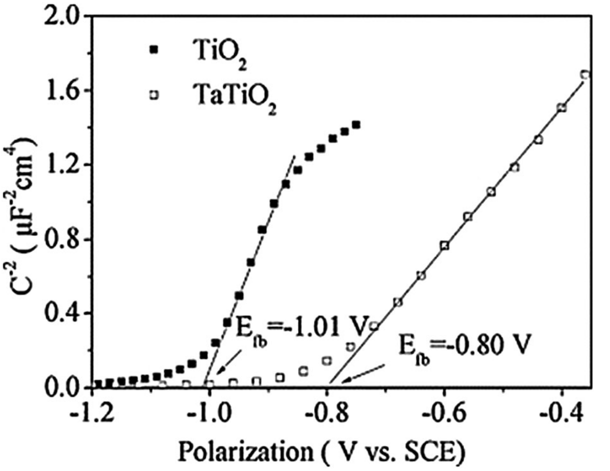

Fig. 11 Mott–Schottky plots for $TiO_2$ and $TaTiO_2$.[193] $V_{FB}$ is given by the intersect of the extrapolated linear regime with the $x$-axis, the electron density by the slope. Reprinted with permission from ref. 283. Copyright 2007 American Chemical Society.

**6.5.7 Charge collection efficiency.** The charge collection efficiency $\eta_{CC}$ is an important parameter as it combines the results of electron transport and lifetime studies, enabling to find the ideal balance between the two. $\eta_{CC}$ is given by[284]

$$\eta_{CC} = 1 - \frac{\tau_{pc}}{\tau_e} = \frac{1}{1 + \tau_{tr}/\tau_n}, \tag{13}$$

provided $\tau_{tr}$ and $\tau_n$ are measured at the same quasi-Fermi level.

A similar parameter is the electron diffusion length

$$L = \sqrt{D_n\tau_n}, \tag{14}$$

which is the average diffusion distance of electrons before they recombine with holes.

## Acknowledgements

This work was supported by the Swiss National Science Foundation under the program NRP70 number 153990 and the European Community's Seventh Framework Programme (FP7/2007–2013) under grant agreement nr. 310184 of the CARINHYPH project.

## References

1 M. Grätzel, *Acc. Chem. Res.*, 2009, **42**(11), 1788–1798.
2 S. Chu and A. Majumdar, *Nature*, 2012, **488**(7411), 294–303.
3 N. S. Lewis and D. G. Nocera, *Proc. Natl. Acad. Sci. U. S. A.*, 2006, **103**(43), 15729–15735.
4 N. Armaroli and V. Balzani, *Angew. Chem., Int. Ed.*, 2007, **46**(1), 52–66.
5 N. S. Lewis, *Science*, 2007, **315**(5813), 798–801.

Open Access Article. Published on 28 August 2015. Downloaded on 2/9/2026 4:13:16 PM.
This article is licensed under a Creative Commons Attribution 3.0 Unported Licence.

6 http://www.nrel.gov/ncpv/images/efficiency_chart.jpg.

7 B. O'Regan and M. Grätzel, *Nature*, 1991, **35**(6346), 737–740.

8 H. J. Snaith and L. Schmidt-Mende, *Adv. Mater.*, 2007, **19**(20), 3187–3200.

9 A. Hagfeldt, G. Boschloo, L. Sun, L. Kloo and H. Pettersson, *Chem. Rev.*, 2010, **110**(11), 6595–6663.

10 M. M. Lee, J. Teuscher, T. Miyasaka, T. N. Murakami and H. J. Snaith, *Science*, 2012, **338**(6107), 643–647.

11 M. Liu, M. B. Johnston and H. J. Snaith, *Nature*, 2013, **501**(7467), 395–398.

12 H.-S. Kim, C.-R. Lee, J.-H. Im, K.-B. Lee, T. Moehl, A. Marchioro, S.-J. Moon, R. Humphry-Baker, J.-H. Yum, J. E. Moser, M. Grätzel and N.-G. Park, *Sci. Rep.*, 2012, **2**, 591.

13 J. Burschka, N. Pellet, S.-J. Moon, R. Humphry-Baker, P. Gao, M. K. Nazeeruddin and M. Grätzel, *Nature*, 2013, **499**(7458), 316–319.

14 R. F. Service, *Science*, 2014, **344**(6183), 458.

15 N. J. Jeon, J. H. Noh, Y. C. Kim, W. S. Yang, S. Ryu and S. I. Seok, *Nat. Mater.*, 2014, **13**(9), 897–903.

16 M. D. McGehee, *Nat. Mater.*, 2014, **13**(9), 845–846.

17 M. Grätzel, *Nat. Mater.*, 2014, **13**(9), 838–842.

18 F. Hao, C. C. Stoumpos, D. H. Cao, R. P. H. Chang and M. G. Kanatzidis, *Nat. Photonics*, 2014, **8**(6), 489–494.

19 N. K. Noel, S. D. Stranks, A. Abate, C. Wehrenfennig, S. Guarnera, A.-A. Haghighirad, A. Sadhanala, G. E. Eperon, S. K. Pathak, M. B. Johnston, A. Petrozza, L. M. Herz and H. J. Snaith, *Energy Environ. Sci.*, 2014, **7**, 3061–3068.

20 A. Mei, X. Li, L. Liu, Z. Ku, T. Liu, Y. Rong, M. Xu, M. Hu, J. Chen, Y. Yang, M. Grätzel and H. Han, *Science*, 2014, **345**(6194), 295–298.

21 H. J. Snaith, A. Abate, J. M. Ball, G. E. Eperon, T. Leijtens, N. K. Noel, S. D. Stranks, J. T.-W. Wang, K. Wojciechowski and W. Zhang, *J. Phys. Chem. Lett.*, 2014, **5**(9), 1511–1515.

22 A. Kojima, K. Teshima, Y. Shirai and T. Miyasaka, *J. Am. Chem. Soc.*, 2009, **131**(17), 6050–6051.

23 J.-H. Im, C.-R. Lee, J.-W. Lee, S.-W. Park and N.-G. Park, *Nanoscale*, 2011, **3**(10), 4088–4093.

24 Z.-S. Wang, H. Kawauchi, T. Kashima and H. Arakawa, *Coord. Chem. Rev.*, 2004, **248**(1314), 1381–1389. Michael Graetzel Festschrift, a tribute for his 60th Birthday, Dye Sensitized Solar Cells.

25 G. K. Mor, O. K. Varghese, M. Paulose, K. Shankar and C. A. Grimes, *Sol. Energy Mater. Sol. Cells*, 2006, **90**(14), 2011–2075.

26 X. Chen and S. S. Mao, *Chem. Rev.*, 2007, **107**(7), 2891–2959.

27 D. Leung, X. Fu, C. Wang, M. Ni, M. Leung, X. Wang and X. Fu, *ChemSusChem*, 2010, **3**(6), 681–694.

28 M. Rauf, M. Meetani and S. Hisaindee, *Desalination*, 2011, **276**(13), 13–27.

29 H. Park, Y. Park, W. Kim and W. Choi, *J. Photochem. Photobiol., C*, 2013, **15**, 1–20.

30 A. K. Chandiran, M. K. Nazeeruddin and M. Grätzel, *Adv. Funct. Mater.*, 2014, **24**(11), 1615–1623.

31 A. Kay and M. Grätzel, *Chem. Mater.*, 2002, **14**(7), 2930–2935.

32 Y. Qiu, W. Chen and S. Yang, *J. Mater. Chem.*, 2010, **20**, 1001–1006.

33 S. H. Ko, D. Lee, H. W. Kang, K. H. Nam, J. Y. Yeo, S. J. Hong, C. P. Grigoropoulos and H. J. Sung, *Nano Lett.*, 2011, **11**(2), 666–671.

34 S. Burnside, J.-E. Moser, K. Brooks, M. Grätzel and D. Cahen, *J. Phys. Chem. B*, 1999, **103**(43), 9328–9332.

35 Y.-C. Nah, I. Paramasivam and P. Schmuki, *ChemPhysChem*, 2010, **11**(13), 2698–2713.

36 A. N. Banerjee, *Nanotechnol., Sci. Appl.*, 2011, **4**, 35–65.

37 G. Li, C. P. Richter, R. L. Milot, L. Cai, C. A. Schmuttenmaer, R. H. Crabtree, G. W. Brudvig and V. S. Batista, *Dalton Trans.*, 2009, 10078–10085.

38 B.-M. Kim, S.-G. Rho and C.-H. Kang, *J. Nanosci. Nanotechnol.*, 2011, **11**(2), 1515–1517.

39 D. O. Scanlon, C. W. Dunnill, J. Buckeridge, S. A. Shevlin, A. J. Logsdail, S. M. Woodley, C. R. A. Catlow, M. J. Powell, R. G. Palgrave, I. P. Parkin, G. W. Watson, T. W. Keal, P. Sherwood, A. Walsh and A. A. Sokol, *Nat. Mater.*, 2013, **12**(9), 798–801.

40 N.-G. Park, J. van de Lagemaat and A. J. Frank, *J. Phys. Chem. B*, 2000, **104**(38), 8989–8994.

41 J. Li, X. Yang, X. Yu, L. Xu, W. Kang, W. Yan, H. Gao, Z. Liu and Y. Guo, *Appl. Surf. Sci.*, 2009, **255**(6), 3731–3738.

42 H.-S. Kim, J.-W. Lee, N. Yantara, P. P. Boix, S. A. Kulkarni, S. Mhaisalkar, M. Grätzel and N.-G. Park, *Nano Lett.*, 2013, **13**(6), 2412–2417.

43 X. Feng, K. Shankar, M. Paulose and C. Grimes, *Angew. Chem.*, 2009, **121**(43), 8239–8242.

44 M. Yang, B. Ding and J.-K. Lee, *J. Power Sources*, 2014, **245**, 301–307.

45 H. Ardakani, *Thin Solid Films*, 1994, **248**(2), 234–239.

46 R. Asahi, Y. Taga, W. Mannstadt and A. Freeman, *Phys. Rev. B: Condens. Matter Mater. Phys.*, 2000, **61**, 7459–7465.

47 A. Paxton and L. Thien-Nga, *Phys. Rev. B: Condens. Matter Mater. Phys.*, 1998, **57**(3), 1579–1584.

48 V. Sivaram, E. J. W. Crossland, T. Leijtens, N. K. Noel, J. Alexander-Webber, P. Docampo and H. J. Snaith, *J. Phys. Chem. C*, 2014, **118**(4), 1821–1827.

49 T. Leijtens, G. E. Eperon, S. Pathak, A. Abate, M. M. Lee and H. J. Snaith, *Nat. Commun.*, 2013, **4**, 2885.

50 S. K. Pathak, A. Abate, T. Leijtens, D. J. Hollman, J. Teuscher, L. Pazos, P. Docampo, U. Steiner and H. J. Snaith, *Adv. Energy Mater.*, 2014, **4**(8), 1301667.

51 S. K. Pathak, A. Abate, P. Ruckdeschel, B. Roose, K. C. Gödel, Y. Vaynzof, A. Santhala, S.-I. Watanabe, D. J. Hollman, N. Noel, A. Sepe, U. Wiesner, R. Friend, H. J. Snaith and U. Steiner, *Adv. Funct. Mater.*, 2014, **24**(38), 6046–6055.

52 J. Bisquert, *J. Phys. Chem. B*, 2004, **108**(7), 2323–2332.

53 M. Adachi, Y. Murata, J. Takao, J. Jiu, M. Sakamoto and F. Wang, *J. Am. Chem. Soc.*, 2004, **126**(45), 14943–14949.

54 G. Schlichthörl, N. G. Park and A. J. Frank, *J. Phys. Chem. B*, 1999, **103**(5), 782–791.

55 G. Franco, J. Gehring, L. M. Peter, E. A. Ponomarev and I. Uhlendorf, *J. Phys. Chem. B*, 1999, **103**(4), 692–698.

56 N. Kopidakis, N. R. Neale, K. Zhu, J. van de Lagemaat and A. J. Frank, *Appl. Phys. Lett.*, 2005, **87**(20), 202106.

Open Access Article. Published on 28 August 2015. Downloaded on 2/9/2026 4:13:16 PM.
This article is licensed under a Creative Commons Attribution 3.0 Unported Licence.

57 J. Bisquert and V. S. Vikhrenko, *J. Phys. Chem. B*, 2004, **108**(7), 2313–2322.

58 M. Radecka, M. Rekas, A. Trenczek-Zajac and K. Zakrzewska, *J. Power Sources*, 2008, **181**(1), 46–55.

59 F. Gu, W. Huang, S. Wang, X. Cheng, Y. Hu and P. S. Lee, *Phys. Chem. Chem. Phys.*, 2014, **16**(47), 25679–25683.

60 M. Yang, D. Kim, H. Jha, K. Lee, J. Paul and P. Schmuki, *Chem. Commun.*, 2011, **47**(7), 2032–2034.

61 X. Peng and A. Chen, *J. Mater. Chem.*, 2004, **14**, 2542–2548.

62 M. Blesic, Z. Saponjic, J. Nedeljkovic and D. Uskokovic, *Mater. Lett.*, 2002, **54**(4), 298–302.

63 X. Wu, Q.-Z. Jiang, Z.-F. Ma, M. Fu and W.-F. Shangguan, *Solid State Commun.*, 2005, **136**(9–10), 513–517.

64 P. S. Archana, A. Gupta, M. M. Yusoff and R. Jose, *Phys. Chem. Chem. Phys.*, 2014, **16**, 7448–7454.

65 D. Xiaoyan, S. Chengwu, Z. Yanru and W. Ni, *J. Semicond.*, 2015, **36**(7), 074003.

66 L. Kavan, N. Tétreault, T. Moehl and M. Grätzel, *J. Phys. Chem. C*, 2014, **118**(30), 16408–16418.

67 Y. Wu, X. Yang, H. Chen, K. Zhang, C. Qin, J. Liu, W. Peng, A. Islam, E. Bi, F. Ye, M. Yin, P. Zhang and L. Han, *Appl. Phys. Express*, 2014, **7**(5), 052301.

68 W. Ke, G. Fang, J. Wang, P. Qin, H. Tao, H. Lei, Q. Liu, X. Dai and X. Zhao, *ACS Appl. Mater. Interfaces*, 2014, **6**(18), 15959–15965.

69 L. Kavan, B. O'Regan, A. Kay and M. Grätzel, *J. Electroanal. Chem.*, 1993, **346**(1), 291–307.

70 J. H. Noh, S. Lee, J. Y. Kim, J.-K. Lee, H. S. Han, C. M. Cho, I. S. Cho, H. S. Jung and K. S. Hong, *J. Phys. Chem. C*, 2009, **113**(3), 1083–1087.

71 S. Lee, J. H. Noh, H. S. Han, D. K. Yim, D. H. Kim, J.-K. Lee, J. Y. Kim, H. S. Jung and K. S. Hong, *J. Phys. Chem. C*, 2009, **113**(16), 6878–6882.

72 R. L. Z. Hoye, K. P. Musselman and J. L. MacManus-Driscoll, *APL Mater.*, 2013, **1**(6), 060701.

73 Y. Duan, N. Fu, Q. Liu, Y. Fang, X. Zhou, J. Zhang and Y. Lin, *J. Phys. Chem. C*, 2012, **116**(16), 8888–8893.

74 F. De Angelis, S. Fantacci, A. Selloni, M. K. Nazeeruddin and M. Gratzel, *J. Phys. Chem. C*, 2010, **114**(13), 6054–6061.

75 S. Meng and E. Kaxiras, *Nano Lett.*, 2010, **10**(4), 1238–1247.

76 C. J. Brinker and G. W. Scherer, *Sol–gel science, the physics and chemistry of sol–gel processing*, Academic Press, Boston, 1990.

77 A. Lamberti, A. Sacco, S. Bianco, D. Manfredi, F. Cappelluti, S. Hernandez, M. Quaglio and C. F. Pirri, *Phys. Chem. Chem. Phys.*, 2013, **15**, 2596–2602.

78 Y. Duan, N. Fu, Q. Zhang, Y. Fang, X. Zhou and Y. Lin, *Electrochim. Acta*, 2013, **107**, 473–480.

79 A. Ahmad, S. Buzby, C. Ni and S. I. Shah, *J. Nanosci. Nanotechnol.*, 2008, **8**(5), 2410–2418.

80 H. Alarcón, M. Hedlund, E. M. J. Johansson, H. Rensmo, A. Hagfeldt and G. Boschloo, *J. Phys. Chem. C*, 2007, **111**(35), 13267–13274.

81 K. H. Ko, Y. C. Lee and Y. J. Jung, *J. Colloid Interface Sci.*, 2005, **283**(2), 482–487.

82 J. Zhang, Z. Han, Q. Li, X. Yang, Y. Yu and W. Cao, *J. Phys. Chem. Solids*, 2011, **72**(11), 1239–1244.

83 S. P. Berglund, S. Hoang, R. L. Minter, R. R. Fullon and C. B. Mullins, *J. Phys. Chem. C*, 2013, **117**(48), 25248–25258.

84 A. Earnshaw and N. Greenwood, *Chemistry of the Elements*, Elsevier Ltd, 2nd edn, 1997.

85 M. Nada, T. Gonda, Q. Shen, H. Shimada, T. Toyoda and N. Kobayashi, *Jpn. J. Appl. Phys.*, 2009, **48**(2R), 025505.

86 A. Subramanian, J. S. Bow and H. W. Wang, *Thin Solid Films*, 2012, **520**(23), 7011–7017.

87 S. Iwamoto, Y. Sazanami, M. Inoue, T. Inoue, T. Hoshi, K. Shigaki, M. Kaneko and A. Maenosono, *ChemSusChem*, 2008, **1**(5), 401–403.

88 K. Kakiage, T. Tokutome, S. Iwamoto, T. Kyomen and M. Hanaya, *Chem. Commun.*, 2013, **49**(2), 179–180.

89 C. Zhang, S. Chen, L. Mo, Y. Huang, H. Tian, L. Hu, Z. Huo, S. Dai, F. Kong and X. Pan, *J. Phys. Chem. C*, 2011, **115**(33), 16418–16424.

90 Q. P. Liu, Y. Zhou, Y. D. Duan, M. Wang and Y. Lin, *Electrochim. Acta*, 2013, **95**, 48–53.

91 Q. Liu, Y. Zhou, Y. duan, M. Wang, X. Zhao and Y. Lin, *J. Alloys Compd.*, 2013, **548**, 161–165.

92 M. Pan, H. Liu, Z. Yao and X. Zhong, *J. Nanomater.*, 2015, **2015**, 974161.

93 W. Li, J. Yang, J. Zhang, S. Gao, Y. Luo and M. Liu, *Mater. Res. Bull.*, 2014, **57**, 177–183.

94 D. F. Watson and G. J. Meyer, *Coord. Chem. Rev.*, 2004, **248**(1314), 1391–1406.

95 K. Kalyanasundaram, *Dye-Sensitized Solar Cells*, EPFL Press, 5th edn, 2010.

96 Z.-L. Jin and G.-X. Lu, *J. Inorg. Mater.*, 2011, **26**(6), 571.

97 H. Tian, L. Hu, C. Zhang, S. Chen, J. Sheng, L. Mo, W. Liu and S. Dai, *J. Mater. Chem.*, 2011, **21**, 863–868.

98 H. Tian, L. Hu, W. Li, J. Sheng, S. Xu and S. Dai, *J. Mater. Chem.*, 2011, **21**, 7074–7077.

99 J. S. Im, J. Yun, S. K. Lee and Y.-S. Lee, *J. Alloys Compd.*, 2012, **513**, 573–579.

100 A. Subramanian and H.-W. Wang, *Appl. Surf. Sci.*, 2012, **258**(17), 6479–6484.

101 T.-V. Nguyen, H.-C. Lee, M. A. Khan and O.-B. Yang, *Sol. Energy*, 2007, **81**(4), 529–534.

102 H. Imahori, S. Hayashi, T. Umeyama, S. Eu, A. Oguro, S. Kang, Y. Matano, T. Shishido, S. Ngamsinlapasathian and S. Yoshikawa, *Langmuir*, 2006, **22**(26), 11405–11411.

103 M. Wang, S. Bai, A. Chen, Y. Duan, Q. Liu, D. Li and Y. Lin, *Electrochim. Acta*, 2012, **77**, 54–59.

104 D. Chen, D. Yang, Q. Wang and Z. Jiang, *Ind. Eng. Chem. Res.*, 2006, **45**(12), 4110–4116.

105 E. Finazzi, C. Di Valentin and G. Pacchioni, *J. Phys. Chem. C*, 2009, **113**(1), 220–228.

106 D. Chu, X. Yuan, G. Qin, M. Xu, P. Zheng, J. Lu and L. Zha, *J. Nanopart. Res.*, 2008, **10**(2), 357–363.

107 C.-W. Hsu, P. Chen and J.-M. Ting, *J. Electrochem. Soc.*, 2013, **160**(3), H160–H165.

108 T. Lindgren, J. M. Mwabora, E. Avendao, J. Jonsson, A. Hoel, C.-G. Granqvist and S.-E. Lindquist, *J. Phys. Chem. B*, 2003, **107**(24), 5709–5716.

Open Access Article. Published on 28 August 2015. Downloaded on 2/9/2026 4:13:16 PM.
This article is licensed under a Creative Commons Attribution 3.0 Unported Licence.

109 X. Wang, Y. Yang, Z. Jiang and R. Fan, *Eur. J. Inorg. Chem.*, 2009, 3481–3487.

110 J. Zhang, Q. Sun, J. Zheng, X. Zhang, Y. Cui, P. Wang, W. Li and Y. Zhu, *J. Renewable Sustainable Energy*, 2011, **3**(3), 033108.

111 J. Zhang, X. Zheng, X. Yang and W. Cao, *J. Inorg. Organomet. Polym. Mater.*, 2011, **21**(1), 150–156.

112 A. A. Umar, M. Y. A. Rahman, S. K. M. Saad and M. M. Salleh, *Int. J. Electrochem. Sci.*, 2012, **7**(9), 7855–7865.

113 W. Liu, Z. Feng and W. Cao, *Res. Chem. Intermed.*, 2013, **39**(4), 1623–1631.

114 H. Diker, C. Varlikli and E. Stathatos, *Int. J. Energy Res.*, 2014, **38**(7), 908–917.

115 D. A. Duarte, M. Massi and A. S. da Silva Sobrinho, *Int. J. Photoenergy*, 2014, 839757.

116 S. P. Lim, A. Pandikumar, N. M. Huang, H. N. Lim, G. Gu and T. L. Ma, *RSC Adv.*, 2014, **4**, 48236–48244.

117 W. Mekprasart, S. Suphankij, T. Tangcharoen, A. Simpraditpan and W. Pecharapa, *Phys. Status Solidi A*, 2014, **211**(8), 1745–1751.

118 O. Simya, M. Selvam, A. Karthik and V. Rajendran, *Synth. Met.*, 2014, **188**, 124–129.

119 R. Kushwaha, R. Chauhan, P. Srivastava and L. Bahadur, *J. Solid State Electrochem.*, 2015, **19**(2), 507–517.

120 X. Zheng, J. Zhang, L. Peng, X. Yang and W. Cao, *J. Mater. Sci.*, 2011, **46**(15), 5071–5078.

121 T. Ma, M. Akiyama, E. Abe and I. Imai, *Nano Lett.*, 2005, **5**(12), 2543–2547. PMID: 16351212.

122 H. Melhem, P. Simon, J. Wang, C. D. Bin, B. Ratier, Y. Leconte, N. Herlin-Boime, M. Makowska-Janusik, A. Kassiba and J. Bouclé, *Sol. Energy Mater. Sol. Cells*, 2013, **117**, 624–631.

123 S. H. Kang, H. S. Kim, J.-Y. Kim and Y.-E. Sung, *Mater. Chem. Phys.*, 2010, **124**(1), 422–426.

124 K. H. Eom, T. K. Yun, J.-Y. Hong, J. Y. Bae, S. Huh and Y. S. Won, *J. Nanosci. Nanotechnol.*, 2014, **14**(12), 9362–9367.

125 W. Guo, Y. Shen, G. Boschloo, A. Hagfeldt and T. Ma, *Electrochim. Acta*, 2011, **56**(12), 4611–4617.

126 Z. Fu, J. Zhang, X. Yang and W. Cao, *Chin. Sci. Bull.*, 2011, **56**(19), 2001–2008.

127 L. Qi, C. Li and Y. Chen, *Chem. Phys. Lett.*, 2012, **539540**, 128–132.

128 Y. Li, L. Jia, C. Wu, S. Han, Y. Gong, B. Chi, J. Pu and L. Jian, *J. Alloys Compd.*, 2012, **512**(1), 23–26.

129 C. K. Lim, H. Huang, C. L. Chow, P. Y. Tan, X. Chen, M. S. Tse and O. K. Tan, *J. Phys. Chem. C*, 2012, **116**(37), 19659–19664.

130 J. Zhang, Z. Fu, Q. Lv, X. Yang and W. Cao, *J. Sol–Gel Sci. Technol.*, 2012, **63**(3), 554–562.

131 W. Qin, S. Lu, X. Wu and S. Wang, *Int. J. Electrochem. Sci.*, 2013, **8**(6), 7984–7990.

132 H. Wang, H. Li, J. Wang, J. Wu, D. Li, M. Liu and P. Su, *Electrochim. Acta*, 2014, **137**, 744–750.

133 W. Guo, L. Wu, Z. Chen, G. Boschloo, A. Hagfeldt and T. Ma, *J. Photochem. Photobiol., A*, 2011, **219**(23), 180–187.

134 W. Guo, Y. Shen, L. Wu, Y. Gao and T. Ma, *J. Phys. Chem. C*, 2011, **115**(43), 21494–21499.

135 T. K. Yun, J. H. Cheon, J. Y. Bae, K.-S. Ahn and J. H. Kim, *J. Nanosci. Nanotechnol.*, 2012, **12**(4), 3305–3308.

136 S. K. Park, T. K. Yun, J. Y. Bae and Y. S. Won, *Appl. Surf. Sci.*, 2013, **285**(part B), 789–794.

137 Y. Xie, N. Huang, Y. Liu, W. Sun, H. F. Mehnane, S. You, L. Wang, W. Liu, S. Guo and X.-Z. Zhao, *Electrochim. Acta*, 2013, **93**, 202–206.

138 J. Huo, Y. Hu, H. Jiang, X. Hou and C. Li, *Chem. Eng. J.*, 2014, **258**, 163–170.

139 M. Motlak, M. S. Akhtar, N. A. Barakat, A. Hamza, O.-B. Yang and H. Y. Kim, *Electrochim. Acta*, 2014, **115**, 493–498.

140 J. Y. Park, K. H. Lee, B. S. Kim, C. S. Kim, S. E. Lee, K. Okuyama, H. D. Jang and T. O. Kim, *RSC Adv.*, 2014, **4**(20), 9946–9952.

141 J. Yu, Y. Yang, R. Fan, L. Li and X. Li, *J. Phys. Chem. C*, 2014, **118**(17), 8795–8802.

142 E. Guo and L. Yin, *Phys. Chem. Chem. Phys.*, 2015, **17**, 563–574.

143 H. Tian, L. Hu, C. Zhang, W. Liu, Y. Huang, L. Mo, L. Guo, J. Sheng and S. Dai, *J. Phys. Chem. C*, 2010, **114**(3), 1627–1632.

144 S. I. Noh, K.-N. Bae, H.-J. Ahn and T.-Y. Seong, *Ceram. Int.*, 2013, **39**(7), 8097–8101.

145 C. Y. Neo and J. Ouyang, *J. Power Sources*, 2013, **241**, 647–653.

146 J. Song, H. B. Yang, X. Wang, S. Y. Khoo, C. C. Wong, X.-W. Liu and C. M. Li, *ACS Appl. Mater. Interfaces*, 2012, **4**(7), 3712–3717.

147 Y. Duan, J. Zheng, M. Xu, X. Song, N. Fu, Y. Fang, X. Zhou, Y. Lin and F. Pan, *J. Mater. Chem. A*, 2015, **3**, 5692–5700.

148 Q. Hou, Y. Zheng, J.-F. Chen, W. Zhou, J. Deng and X. Tao, *J. Mater. Chem.*, 2011, **21**(11), 3877–3883.

149 S. Tojo, T. Tachikawa, M. Fujitsuka and T. Majima, *J. Phys. Chem. C*, 2008, **112**(38), 14948–14954.

150 G. Liu, C. Sun, X. Yan, L. Cheng, Z. Chen, X. Wang, L. Wang, S. C. Smith, G. Q. M. Lu and H.M. Cheng, *J. Mater. Chem.*, 2009, **19**, 2822–2829.

151 M. Niu, R. Cui, H. Wu, D. Cheng and D. Cao, *J. Phys. Chem. C*, 2015, **119**(24), 13425–13432.

152 A. Latini, C. Cavallo, F. K. Aldibaja, D. Gozzi, D. Carta, A. Corrias, L. Lazzarini and G. Salviati, *J. Phys. Chem. C*, 2013, **117**(48), 25276–25289.

153 Z. Liu, Y. Li, C. Liu, J. Ya, E. Lei, W. Zhao, D. Zhao and L. An, *ACS Appl. Mater. Interfaces*, 2011, **3**(5), 1721–1725.

154 J. Liu, Y. Duan, X. Zhou and Y. Lin, *Appl. Surf. Sci.*, 2013, **277**, 231–236.

155 H. Seo, Y. Wang, D. Ichida, G. Uchida, N. Itagaki, K. Koga, M. Shiratani, S.-H. Nam and J.-H. Boo, *Jpn. J. Appl. Phys.*, 2013, **52**(11S), 11NM02.

156 Y. Xie, N. Huang, S. You, Y. Liu, B. Sebo, L. Liang, X. Fang, W. Liu, S. Guo and X.-Z. Zhao, *J. Power Sources*, 2013, **224**, 168–173.

157 M. R. Mohammadi, A. M. Bakhshayesh, F. Sadri and M. Masroor, *J. Sol–Gel Sci. Technol.*, 2013, **67**(1), 77–87.

158 C. Kim, K. S. Kim, H. Y. Kim and Y. S. Han, *J. Mater. Chem.*, 2008, **18**(47), 5809–5814.

Open Access Article. Published on 28 August 2015. Downloaded on 2/9/2026 4:13:16 PM.
This article is licensed under a Creative Commons Attribution 3.0 Unported Licence.

159 L. C.-K. Liau and C.-C. Lin, *Thin Solid Films*, 2008, **516**(8), 1998–2002.

160 A. Shalan and M. Rashad, *Appl. Surf. Sci.*, 2013, **283**, 975–981.

161 S. G. Shin, C. W. Bark and H. W. Choi, *Mol. Cryst. Liq. Cryst.*, 2014, **600**(1), 47–55.

162 B. Yacoubi, L. Samet, J. Bennaceur, A. Lamouchi and R. Chtourou, *Mater. Sci. Semicond. Process.*, 2015, **30**, 361–367.

163 T. S. Eom, K. H. Kim, C. W. Bark and H. W. Choi, *Mol. Cryst. Liq. Cryst.*, 2014, **600**(1), 39–46.

164 L. C.-K. Liau and C.-C. Lin, *Appl. Surf. Sci.*, 2007, **253**(21), 8798–8801.

165 P. S. Archana, E. Naveen Kumar, C. Vijila, S. Ramakrishna, M. M. Yusoff and R. Jose, *Dalton Trans.*, 2013, **42**, 1024–1032.

166 A. Malik, S. Hameed, M. J. Siddiqui, M. M. Haque, K. Umar, A. Khan and M. Muneer, *J. Mater. Eng. Perform.*, 2014, **23**(9), 3184–3192.

167 S. N. F. Zainudin, M. Markom, H. Abdullah, *Advanced Materials Conference (AMS 2012)*, 2014, 879, 199–205.

168 T. R. C. K. Wijayarathna, G. M. L. P. Aponsu, Y. P. Y. P. Ariyasinghe, E. V. A. Premalal, G. K. R. Kumara and K. Tennakone, *Nanotechnology*, 2008, **19**(48), 485703.

169 J. Navas, C. Fernandez-Lorenzo, T. Aguilar, R. Alcantara and J. Martin-Calleja, *Phys. Status Solidi A*, 2012, **209**(2), 378–385.

170 Y. Wang, Y. Hao, H. Cheng, J. Ma, B. Xu, W. Li and S. Cai, *J. Mater. Sci.*, 1999, **34**(12), 2773–2779.

171 J. C. Zhang, C. Y. Fu, X. Y. Yang and W. L. Cao, *J. Inorg. Organomet. Polym. Mater.*, 2011, **21**(1), 43–49.

172 K.-P. Wang and H. Teng, *Phys. Chem. Chem. Phys.*, 2009, **11**(41), 9489–9496.

173 Y. Zhang, L. Wang, B. Liu, J. Zhai, H. Fan, D. Wang, Y. Lin and T. Xie, *Electrochim. Acta*, 2011, **56**(18), 6517–6523.

174 X. Zhang, S.-T. Wang and Z.-S. Wang, *Appl. Phys. Lett.*, 2011, **99**(11), 113503.

175 F. Zhu, P. Zhang, X. Wu, L. Fu, J. Zhang and D. Xu, *ChemPhysChem*, 2012, **13**(16), 3731–3737.

176 G. Zhu, Z. Cheng, T. Lv, L. Pan, Q. Zhao and Z. Sun, *Nanoscale*, 2010, **2**(7), 1229–1232.

177 A. H. G. Niaki, A. M. Bakhshayesh and M. R. Mohammadi, *Sol. Energy*, 2014, **103**, 210–222.

178 Z. Ali, K. H. Park, I. Shakir and D. J. Kang, *Electrochim. Acta*, 2015, **161**, 329–334.

179 S. Chen, J. Lin and J. Wu, *Appl. Surf. Sci.*, 2014, **293**, 202–206.

180 S. Chen, J. Lin and J. Wu, *J. Mater. Sci.*, 2014, **25**(5), 2060–2065.

181 A. K. Chandiran, F. Sauvage, L. Etgar and M. Grätzel, *J. Phys. Chem. C*, 2011, **115**(18), 9232–9240.

182 A. Kitiyanan, S. Ngamsinlapasathian, S. Pavasupree and S. Yoshikawa, *J. Solid State Chem.*, 2005, **178**(4), 1044–1048.

183 M. Dürr, S. Rosselli, A. Yasuda and G. Nelles, *J. Phys. Chem. B*, 2006, **110**(43), 21899–21902.

184 P. S. Archana, A. Gupta, M. M. Yusoff and R. Jose, *Appl. Phys. Lett.*, 2014, **105**(15), 153901.

185 P. S. Archana, R. Jose, T. M. Jin, C. Vijila, M. M. Yusoff and S. Ramakrishna, *J. Am. Ceram. Soc.*, 2010, **93**(12), 4096–4102.

186 X. Lü, X. Mou, J. Wu, D. Zhang, L. Zhang, F. Huang, F. Xu and S. Huang, *Adv. Funct. Mater.*, 2010, **20**(3), 509–515.

187 N. Tsvetkov, L. Larina, O. Shevaleevskiy and B. T. Ahn, *Energy Environ. Sci.*, 2011, **4**(4), 1480–1486.

188 N. Tsvetkov, L. Larina, O. Shevaleevskiy and B. Ahn, *J. Electrochem. Soc.*, 2011, **158**(11), B1281–B1285.

189 S. G. Kim, M. J. Ju, I. T. Choi, W. S. Choi, H. J. Choi, J. B. Baek and H. K. Kim, *RSC Adv.*, 2013, **3**(37), 16380–16386.

190 A. K. Chandiran, F. Sauvage, M. Casas-Cabanas, P. Comte, S. M. Zakeeruddin and M. Grätzel, *J. Phys. Chem. C*, 2010, **114**(37), 15849–15856.

191 L. Long, L. Wu, X. Yang and X. Li, *J. Mater. Sci. Technol.*, 2014, **30**(8), 765–769.

192 J. Luo, J. Zhou, H. Guo, W. Yang, B. Liao, W. Shi and Y. Chen, *RSC Adv.*, 2014, **4**, 56318–56322.

193 J. Liu, H. Yang, W. Tan, X. Zhou and Y. Lin, *Electrochim. Acta*, 2010, **56**(1), 396–400.

194 J. H. Choi, S. H. Kwon, Y. K. Jeong, I. Kim and K. H. Kim, *J. Electrochem. Soc.*, 2011, **158**(6), 749–753.

195 R. Ghosh, Y. Hara, L. Alibabaei, K. Hanson, S. Rangan, R. Bartynski, T. J. Meyer and R. Lopez, *ACS Appl. Mater. Interfaces*, 2012, **4**(9), 4566–4570.

196 M.-C. Kao, H.-Z. Chen and S.-L. Young, *Jpn. J. Appl. Phys.*, 2013, **52**(1S), 01AD04.

197 K. Lee and P. Schmuki, *Electrochem. Commun.*, 2012, **25**, 11–14.

198 X. Zhang, F. Liu, Q.-L. Huang, G. Zhou and Z.-S. Wang, *J. Phys. Chem. C*, 2011, **115**(25), 12665–12671.

199 H. Kamisaka, T. Suenaga, H. Nakamura and K. Yamashita, *J. Phys. Chem. C*, 2010, **114**(29), 12777–12783.

200 A. M. Cant, F. Z. Huang, X. L. Zhang, Y. Chen, Y. B. Cheng and R. Amal, *Nanoscale*, 2014, **6**(7), 3875–3880.

201 J. H. Yang, K. H. Kim, C. W. Bark and H. W. Choi, *Mol. Cryst. Liq. Cryst.*, 2014, **598**(1), 32–39.

202 Z. Tong, T. Peng, W. Sun, W. Liu, S. Guo and X.-Z. Zhao, *J. Phys. Chem. C*, 2014, **118**(30), 16892–16895.

203 M. Grätzel, *Nature*, 2001, **414**(6861), 338–344.

204 Y. Furubayashi, T. Hitosugi, Y. Yamamoto, K. Inaba, G. Kinoda, Y. Hirose, T. Shimada and T. Hasegawa, *Appl. Phys. Lett.*, 2005, **86**(25), 252101.

205 M. Hirano and K. Matsushima, *J. Nanosci. Nanotechnol.*, 2006, **6**(3), 762–770.

206 X.-G. Hou, A.-D. Liu, M.-D. Huang, B. Liao and X.-L. Wu, *Chin. Phys. Lett.*, 2009, **26**(7), 077106.

207 L. Kavan, M. Grätzel, S. E. Gilbert, C. Klemenz and H. J. Scheel, *J. Am. Chem. Soc.*, 1996, **118**(28), 6716–6723.

208 F. Huang, Y.-B. Cheng and R. Caruso, *Aust. J. Chem.*, 2011, **64**(6), 820–824.

209 K. Manoharan and P. Venkatachalam, *Mater. Sci. Semicond. Process.*, 2015, **30**, 208–217.

210 A. Bakhshayesh and N. Farajisafiloo, *Appl. Surf. Sci.*, 2015, **331**, 58–65.

211 X. H. Sun, Q. L. Zhang, Y. M. Liu, N. Huang, P. P. Sun, T. Peng, T. Y. Peng and X. Z. Zhao, *Electrochim. Acta*, 2014, **129**, 276–282.

Open Access Article. Published on 28 August 2015. Downloaded on 2/9/2026 4:13:16 PM.
This article is licensed under a Creative Commons Attribution 3.0 Unported Licence.

212 S. Yun, J. Lee, J. Chung and S. Lim, *J. Phys. Chem. Solids*, 2010, **71**(12), 1724–1731.

213 J. Augustynski, J. Hinden and C. Stalder, *J. Electrochem. Soc.*, 1977, **124**(7), 1063–1064.

214 P. Strange, A. Svane, W. M. Temmerman, Z. Szotek and H. Winter, *Nature*, 1999, **399**(6738), 756–758.

215 F. Auzel, *Chem. Rev.*, 2004, **104**(1), 139–174.

216 C. Strümpel, M. McCann, G. Beaucarne, V. Arkhipov, A. Slaoui, V. Svrcek, C. del Canizo and I. Tobias, *Sol. Energy Mater. Sol. Cells*, 2007, **91**(4), 238–249.

217 J. Wang, T. Ming, Z. Jin, J. Wang, L.-D. Sun and C.-H. Yan, *Nat. Commun.*, 2014, **5**, 5669.

218 Y. Masuda, M. Yamagishi and K. Koumoto, *Chem. Mater.*, 2007, **19**(5), 1002–1008.

219 X.-H. Wu, S. Wang, Y. Guo, Z.-Y. Xie, L. Han and Z.-H. Jiang, *Chin. J. Chem.*, 2008, **26**(10), 1939–1943.

220 J. Zhang, Z. Zhao, X. Wang, T. Yu, J. Guan, Z. Yu, Z. Li and Z. Zou, *J. Phys. Chem. C*, 2010, **114**(43), 18396–18400.

221 S. Yahav, S. Rühle, S. Greenwald, H.-N. Barad, M. Shalom and A. Zaban, *J. Phys. Chem. C*, 2011, **115**(43), 21481–21486.

222 J. Zhang, W. Peng, Z. Chen, H. Chen and L. Han, *J. Phys. Chem. C*, 2012, **116**(36), 19182–19190.

223 J. Zhang, J. Feng, Y. Hong, Y. Zhu and L. Han, *J. Power Sources*, 2014, **257**, 264–271.

224 Q. Yao, J. Liu, Q. Peng, X. Wang and Y. Li, *Chem. – Asian J.*, 2006, **1**(5), 737–741.

225 H. Hafez, M. Saif and M. Abdel-Mottaleb, *J. Power Sources*, 2011, **196**(13), 5792–5796.

226 Q. B. Li, J. M. Lin, J. H. Wu, Z. Lan, Y. Wang, F. G. Peng and M. L. Huang, *J. Lumin.*, 2013, **134**, 59–62.

227 H. Hafez, J. Wu, Z. Lan, Q. Li, G. Xie, J. Lin, M. Huang, Y. Huang and M. S. Abdel-Mottaleb, *Nanotechnology*, 2010, **21**(41), 415201.

228 J. Wu, G. Xie, J. Lin, Z. Lan, M. Huang and Y. Huang, *J. Power Sources*, 2010, **195**(19), 6937–6940.

229 S. H. Huang, *J. Am. Ceram. Soc.*, 2013, **96**(10), 3108–3113.

230 J. H. Wu, J. L. Wang, J. M. Lin, Y. M. Xiao, G. T. Yue, M. L. Huang, Z. Lan, Y. F. Huang, L. Q. Fan, S. Yin and T. Sato, *Sci. Rep.*, 2013, **3**, 5.

231 G.-B. Shan and G. P. Demopoulos, *Adv. Mater.*, 2010, **22**(39), 4373–4377.

232 G. X. Xie, J. M. Lin, J. H. Wu, Z. Lan, Q. H. Li, Y. M. Xiao, G. T. Yue, H. F. Yue and M. L. Huang, *Chin. Sci. Bull.*, 2011, **56**(1), 96–101.

233 J. L. Wang, J. H. Wu, J. M. Lin, M. L. Huang, Y. F. Huang, Z. Lan, Y. M. Xiao, G. T. Yue, S. Yin and T. Sato, *ChemSusChem*, 2012, **5**(7), 1307–1312.

234 J. Wu, J. Wang, J. Lin, Z. Lan, Q. Tang, M. Huang, Y. Huang, L. Fan, Q. Li and Z. Tang, *Adv. Energy Mater.*, 2012, **2**(1), 78–81.

235 J. L. Wang, J. M. Lin, J. H. Wu, M. L. Huang, Z. Lan, Y. Chen, S. Tang, L. Q. Fan and Y. F. Huang, *Electrochim. Acta*, 2012, **70**, 131–135.

236 J. Yu, Y. Yang, R. Fan, H. Zhang, L. Li, L. Wei, Y. Shi, K. Pan and H. Fu, *J. Power Sources*, 2013, **243**, 436–443.

237 Q. B. Li, J. M. Lin, J. H. Wu, Z. Lan, Y. Wang, F. G. Peng and M. L. Huang, *Electrochim. Acta*, 2011, **56**(14), 4980–4984.

238 G. X. Xie, Y. L. Wei, L. Q. Fan and J. H. Wu, *J. Phys.: Conf. Ser.*, 2012, **339**(1), 012010.

239 W.-W. Xu, S.-Y. Dai, L.-H. Hu, L.-Y. Liang and K.-J. Wang, *Chin. Phys. Lett.*, 2006, **23**(8), 2288.

240 J. Liqiang, S. Xiaojun, X. Baifu, W. Baiqi, C. Weimin and F. Honggang, *J. Solid State Chem.*, 2004, **177**(10), 3375–3382.

241 S. W. Chen, J. M. Lee, K. T. Lu, C. W. Pao, J. F. Lee, T. S. Chan and J. M. Chen, *Appl. Phys. Lett.*, 2010, **97**(1), 012104.

242 G. E. Eperon, V. M. Burlakov, P. Docampo, A. Goriely and H. J. Snaith, *Adv. Funct. Mater.*, 2014, **24**(1), 151–157.

243 J. Wang, M. Qin, H. Tao, W. Ke, Z. Chen, J. Wan, P. Qin, L. Xiong, H. Lei, H. Yu and G. Fang, *Appl. Phys. Lett.*, 2015, **106**(12), 121104.

244 D. H. Kim, G. S. Han, W. M. Seong, J.-W. Lee, B. J. Kim, N.-G. Park, K. S. Hong, S. Lee and H. S. Jung, *ChemSusChem*, 2015, **8**(14), 2392–2398.

245 T. Oku, T. Iwata and A. Suzuki, *Chem. Lett.*, 2015, **44**(7), 1033–1035.

246 P. Qin, A. L. Domanski, A. K. Chandiran, R. Berger, H.-J. Butt, M. I. Dar, T. Moehl, N. Tetreault, P. Gao, S. Ahmad, M. K. Nazeeruddin and M. Gratzel, *Nanoscale*, 2014, **6**, 1508–1514.

247 H. Zhou, Q. Chen, G. Li, S. Luo, T.-b. Song, H.-S. Duan, Z. Hong, J. You, Y. Liu and Y. Yang, *Science*, 2014, **345**(6196), 542–546.

248 H. Nagaoka, F. Ma, D. W. deQuilettes, S. M. Vorpahl, M. S. Glaz, A. E. Colbert, M. E. Ziffer and D. S. Ginger, *J. Phys. Chem. Lett.*, 2015, **6**(4), 669–675.

249 C. Wehrenfennig, M. Liu, H. J. Snaith, M. B. Johnston and L. M. Herz, *Energy Environ. Sci.*, 2014, **7**, 2269–2275.

250 H.-W. Chen, N. Sakai, M. Ikegami and T. Miyasaka, *J. Phys. Chem. Lett.*, 2015, **6**(1), 164–169.

251 E. L. Unger, E. T. Hoke, C. D. Bailie, W. H. Nguyen, A. R. Bowring, T. Heumuller, M. G. Christoforo and M. D. McGehee, *Energy Environ. Sci.*, 2014, **7**, 3690–3698.

252 H.-S. Kim, I. Mora-Sero, V. Gonzalez-Pedro, F. Fabregat-Santiago, E. J. Juarez-Perez, N.-G. Park and J. Bisquert, *Nat. Commun.*, 2013, **4**, 2242.

253 A. Dualeh, T. Moehl, N. Tétreault, J. Teuscher, P. Gao, M. K. Nazeeruddin and M. Grätzel, *ACS Nano*, 2014, **8**(1), 362–373.

254 H.-S. Kim and N.-G. Park, *J. Phys. Chem. Lett.*, 2014, **5**(17), 2927–2934.

255 W. Tress, N. Marinova, T. Moehl, S. M. Zakeeruddin, M. K. Nazeeruddin and M. Grätzel, *Energy Environ. Sci.*, 2015, **8**, 995–1004.

256 Y. Shao, Z. Xiao, C. Bi, Y. Yuan and J. Huang, *Nat. Commun.*, 2014, **5**, 5784.

257 M. H. N. Assadi and D. A. H. Hanaor, *J. Appl. Phys.*, 2013, **113**(23), 233913.

258 H. M. Rietveld, *J. Appl. Crystallogr.*, 1969, **2**(2), 65–71.

259 P. Scherrer, *Göttinger Nachrichten Gesell.*, 1918, **2**, 98.

260 A. Patterson, *Phys. Rev.*, 1939, **56**, 978–982.

261 W. L. Bragg, *Proc. Cambridge Philos. Soc.*, 1913, **17**, 43–57.

Open Access Article. Published on 28 August 2015. Downloaded on 2/9/2026 4:13:16 PM. This article is licensed under a Creative Commons Attribution 3.0 Unported Licence.

262 M. Gaudon, O. Toulemonde and A. Demourgues, *Inorg. Chem.*, 2007, **46**(26), 10996–11002.

263 A. Denton and N. Ashcroft, *Phys. Rev. A: At., Mol., Opt. Phys.*, 1991, **43**, 3161–3164.

264 S. Brunauer, P. H. Emmett and E. Teller, *J. Am. Chem. Soc.*, 1938, **60**(2), 309–319.

265 E. P. Barrett, L. G. Joyner and P. P. Halenda, *J. Am. Chem. Soc.*, 1951, **73**(1), 373–380.

266 A. Escobedo Morales and E. P. U. Sánchez Mora, *Suppl. to Revista Mexicana de Fisica*, 2007, **53**(5), 18–22.

267 P. Kubelka and F. Munk, *Z. Tech. Phys.*, 1931, **12**, 593–601.

268 J. Tauc, *Mater. Res. Bull.*, 1968, **3**(1), 37–46.

269 B. Choudhury and A. Choudhury, *Mater. Chem. Phys.*, 2012, **132**(23), 1112–1118.

270 H. Alarcón, G. Boschloo, P. Mendoza, J. L. Solis and A. Hagfeldt, *J. Phys. Chem. B*, 2005, **109**(39), 18483–18490.

271 E. H. Hall, *Am. J. Math.*, 1879, **2**(3), 287–292.

272 R. S. Popovic, *Hall Effect Devices: Magnetic Sensors and Characterization of Semiconductors (Series in Sensors)*, Taylor & Francis, 1991.

273 D. Hurum, A. Agrios, S. Crist, K. Gray, T. Rajh and M. Thurnauer, *J. Electron Spectrosc. Relat. Phenom.*, 2006, **150**(2-3), 155–163.

274 P. R. F. Barnes, K. Miettunen, X. Li, A. Y. Anderson, T. Bessho, M. Grätzel and B. C. O'Regan, *Adv. Mater.*, 2013, **25**(13), 1881–1922.

275 S. Sarker, A. J. S. Ahammad, H. W. Seo and D. M. Kim, *Int. J. Photoenergy*, 2014, 851705.

276 F. Cao, G. Oskam, G. J. Meyer and P. C. Searson, *J. Phys. Chem.*, 1996, **100**(42), 17021–17027.

277 J. van de Lagemaat and A. J. Frank, *J. Phys. Chem. B*, 2001, **105**(45), 11194–11205.

278 G. Schlichthörl, S. Y. Huang, J. Sprague and A. J. Frank, *J. Phys. Chem. B*, 1997, **101**(41), 8141–8155.

279 A. Zaban, M. Greenshtein and J. Bisquert, *ChemPhysChem*, 2003, **4**(8), 859–864.

280 G. Boschloo, L. Häggman and A. Hagfeldt, *J. Phys. Chem. B*, 2006, **110**(26), 13144–13150.

281 G. Boschloo and A. Hagfeldt, *J. Phys. Chem. B*, 2005, **109**(24), 12093–12098.

282 B. C. O'Regan, S. Scully, A. C. Mayer, E. Palomares and J. Durrant, *J. Phys. Chem. B*, 2005, **109**(10), 4616–4623.

283 K. Gelderman, L. Lee and S. W. Donne, *J. Chem. Educ.*, 2007, **84**(4), 685.

284 J. van de Lagemaat, N.-G. Park and A. J. Frank, *J. Phys. Chem. B*, 2000, **104**(9), 2044–2052.